Carbohydrate Polymers

Understanding the mechanisms of enantiomer binding and recognition with cyclodextrins by integrating capillary electrophoresis, nuclear magnetic resonance and quantum mechanics

--Manuscript Draft--

Manuscript Number:	
Article Type:	Research Paper
Keywords:	Capillary electrophoresis; Cyclodextrins; Enantioseparation; Molecular modeling; Tetramisole
Corresponding Author:	Bezhan Chankvetadze, PhD Ivane Javakhishvili Tbilisi State University Faculty of Exact and Natural Sciences Muenster, GERMANY
First Author:	Bezhan Chankvetadze, PhD
Order of Authors:	Bezhan Chankvetadze, PhD
	Ani Rurua
	Mariam Shanidze
	Nutsa Tsetskhladze
	Antonio Salgado
	Paola Peluso, PhD
	Roberto Dallocchio
	Gerhard K.E. Scriba, PhD
	Milo Malanga, PhD
	Szabolcs Beni, PhD
Abstract:	Multiple factors may impact enantiorecognition ability of CDs, and the validation of computational tools by using suitable experimental data is a critical point. The main advantage of using capillary electrophoresis (CE) for this purpose relies on its higher sensitivity to detect weak noncovalent intermolecular interactions compared to any other technique. In this study, we used CE enantioseparations of tetramisole with β-CD, heptakis(2,3-di-O-methyl)-β-CD, heptakis(2,3-di-O-acetyl)-β-CD and heptakis(2-O-methyl-3-O-acetyl)-β-CD as benchmark separation systems aiming at investigating the molecular bases of these processes by NMR spectroscopy and quantum mechanics (QM) methods. The aim of this study was explaining the subtle differences observed in enantiomer migration order, that means enantiomer affinity pattern of tetramisole toward the used CDs, migration times, and selectivity values. A good correlation between experimental and theoretical data was obtained along with noncovalent interactions patterns fully consistent with the CE outcomes. Significant differences in the enantioselective recognition ability were observed between β-CD and heptakis(2,3-di-O-acetyl)-β-CD in CE, which correlated very well with the recognition model derived from NMR spectroscopy and QM. Importantly, the introduction of dispersion corrections in the used QM model chemistry provided results in better agreement with the experimental observations for the complexes of tetramisole with the acetylated β-CDs.

Understanding the mechanisms of enantiomer binding and recognition with cyclodextrins by integrating capillary electrophoresis, nuclear magnetic resonance and quantum mechanics

Ani Rurua [a], Mariam Shanidze [a], Nutsa Tsetskhladze [a], Antonio Salgado [b], Paola Peluso [c,*], Roberto Dallocchio [c], Gerhard K.E. Scriba [a,d], Milo Malanga [e], Szabolcs Beni [f], Bezhan Chankvetadze [a,*]

[a] Institute of Physical and Analytical Chemistry, School of Exact and Natural Sciences, Tbilisi State University, Chavchavadze Ave 3, Tbilisi 0179, Georgia

[b] NMR Spectroscopy Centre (CERMN), Faculty of Pharmacy, University of Alcalá, CAI Químicas, 28805 Alcalá de Henares, Madrid, Spain

[c] Institute of Biomolecular Chemistry ICB, CNR, Traversa La Crucca 3, Li Punti, Sassari 07100, Italy

[d] Friedrich-Schiller-University Jena, Department of Pharmaceutical/Medicinal Chemistry, Philosophenweg 14, 07743 Jena, Germany

[e] CarboHyde Zrt., Berlini u. 47-49, 1045 Budapest, Hungary

[f] Integrative Health and Environmental Analysis Research Laboratory, Department of Analytical Chemistry, Institute of Chemistry, Eötvös Loránd University, 1117 Budapest, Hungary

Corresponding authors: Prof. Bezhan Chankvetadze, e-mail: jpba_bezhan@yahoo.com;
Dr. Paola Peluso, e-mail: paola.peluso@cnr.it

Keywords: Capillary electrophoresis / Cyclodextrins / Enantioseparation / Molecular modeling / Tetramisole

Abstract

Multiple factors may impact enantiorecognition ability of CDs, and the validation of computational tools by using suitable experimental data is a critical point. The main advantage of using capillary electrophoresis (CE) for this purpose relies on its higher sensitivity to detect weak noncovalent intermolecular interactions compared to any other technique. In this study, we used CE enantioseparations of tetramisole with β-CD, *heptakis*(2,3-di-*O*-methyl)-β-CD, *heptakis*(2,3-di-*O*-acetyl)-β-CD and *heptakis*(2-*O*-methyl-3-*O*-acetyl)-β-CD as benchmark separation systems aiming at investigating the molecular bases of these processes by NMR spectroscopy and quantum mechanics (QM) methods. The aim of this study was explaining the subtle differences observed in enantiomer migration order, that means enantiomer affinity pattern of tetramisole toward the used CDs, migration times, and selectivity values. A good correlation between experimental and theoretical data was obtained along with noncovalent interactions patterns fully consistent with the CE outcomes. Significant differences in the enantioselective recognition ability were observed between β-CD and *heptakis*(2,3-di-*O*-acetyl)-β-CD in CE, which correlated very well with the recognition model derived from NMR spectroscopy and QM. Importantly, the introduction of dispersion corrections in the used QM model chemistry provided results in better agreement with the experimental observations for the complexes of tetramisole with the acetylated β-CDs.

Highlights

- CE enantioseparation of tetramisole with β-CD and derivatives
- Study of native and derivatized β-CDs by quantum mechanics
- Comparison of molecular and electronic features of β-CD and derivatized β-CDs
- A study of binding and recognition mechanisms using CE, NMR and QM

1 Introduction

Noncovalent intermolecular interactions play an important role in chemistry, biology, medicine and in nature in general (Peluso & Chankvetadze, 2022). In the last decades, intensive research has been dedicated to the understanding of the function and role of noncovalent interactions in binding and recognition mechanisms by integrating experimental and computational analyses. Despite intensive research in this field, noncovalent interactions are currently less understood compared to covalent bonds (Schneider, 2019; Schneider, 2022). In chemistry, one of the fields in which noncovalent intermolecular interactions play a significant role among others is enantioselective selector-selectand recognition. This, on its own, finds a reflection in fields such as enantioselective catalysis, enantiomer separation, and interaction of chiral drugs with their receptors in a living body. Current tools of theoretical chemistry are frequently used for modeling and rationalizing interactions of chiral selectands with chiral selectors (Dallocchio et al., 2023; Peluso et al., 2019; Sardella et al., 2020; Varfaj et al., 2024). However, most often, modeled results lack experimental confirmation (Chankvetadze & Scriba, 2023; Peluso & Chankvetadze, 2021). This is a big issue because a model computed for a given real molecular system without experimental validation remains, as a matter of fact, in the boundaries of theoretical speculation. In other words, considering a computed model *a priori* to describe a real system in a valid manner is fundamentally incorrect because no efforts are undertaken to identify, correct, and overcome possible pitfalls of theory. Therefore, over many years we have promoted the application of computational and experimental tools in parallel to further refine computations for a proper description of noncovalent interactions (Chankvetadze et al., 2002; Peluso et al., 2023; Peluso et al., 2024; Salgado et al., 2017). Among the experimental methods currently available, together with various spectroscopic techniques such as Nuclear Magnetic Resonance (NMR) spectroscopy (Chankvetadze, 2004; Salgado & Chankvetadze, 2016), mass spectrometry (Casas-Hinestroza et al., 2019; Chen et al., 2016) and several others, separation science techniques are especially useful for studying noncovalent intermolecular interactions. Due to their cumulative character, they enable the detection of very weak (enantioselective) noncovalent interactions, which may be easily overlooked by other methods (Blaschke & Chankvetadze, 2000; Chankvetadze, 2004; Peluso & Chankvetadze, 2022). From this viewpoint, capillary electrophoresis (CE) is a specifically powerful method (Chankvetadze, 1999; Chankvetadze, 2004; Chankvetadze & Blaschke, 2001). Furthermore, CE is a miniaturized technique and does not require ligand (selectand) or receptor (selector) immobilization.

Native cyclodextrins (CDs) and their derivatives are widely used in CE enantioseparations as chiral selectors. On the other hand, the application of CE for the detection of the effects of structural changes in the CD-type chiral selectors on their enantioselective recognition ability and pattern has been systematically reported in the last 25 years (Chankvetadze et al., 1999; Chankvetadze et al., 2000; Chankvetadze et al., 2002; Chankvetadze & Scriba, 2023; Gogolashvili et al., 2021; Peluso & Chankvetadze, 2021). In this field, the abovementioned high sensitivity of CE for the detection of very weak intermolecular interactions, is, at the same time, a big challenge for computational techniques. The enantioselective recognition detected with CE is based on Gibbs free energy differences in the range of few tens of $cal \cdot mol^{-1}$. Reliable modeling of such small energy differences is very challenging with the computational tools currently available, and, in several cases, computation results of

CD/enantiomer complexes provide binding free energy values (Mazurek & Szeleszczuk, 2022; Silva et al., 2020) more negative than the corresponding values derived from the experimental separation factor (α). In the best case, only a qualitative correlation between computed energies and experimental data can be established. Thus, there is an urgent need to refine the computational tools we have at disposal to date in order to make them able to adequately model weak noncovalent interactions and related enantioselective processes.

In the present study, we examined CE enantioseparation of tetramisole (2,3,5,6-tetrahydro-6-phenylimidazo[2,1-b]thiazole, Figure 1A) using β-CD and three 2,3-disubstituted β-CD derivatives (Figure 1B), *heptakis*(2,3-di-*O*-methyl)-β-CD (HDM-β-CD), *heptakis*(2,3-di-*O*-acetyl)-β-CD (HDA-β-CD), and *heptakis*(2-*O*-methyl-3-*O*-acetyl)-β-CD (HMA-β-CD), as chiral selectors (Figure 1C).

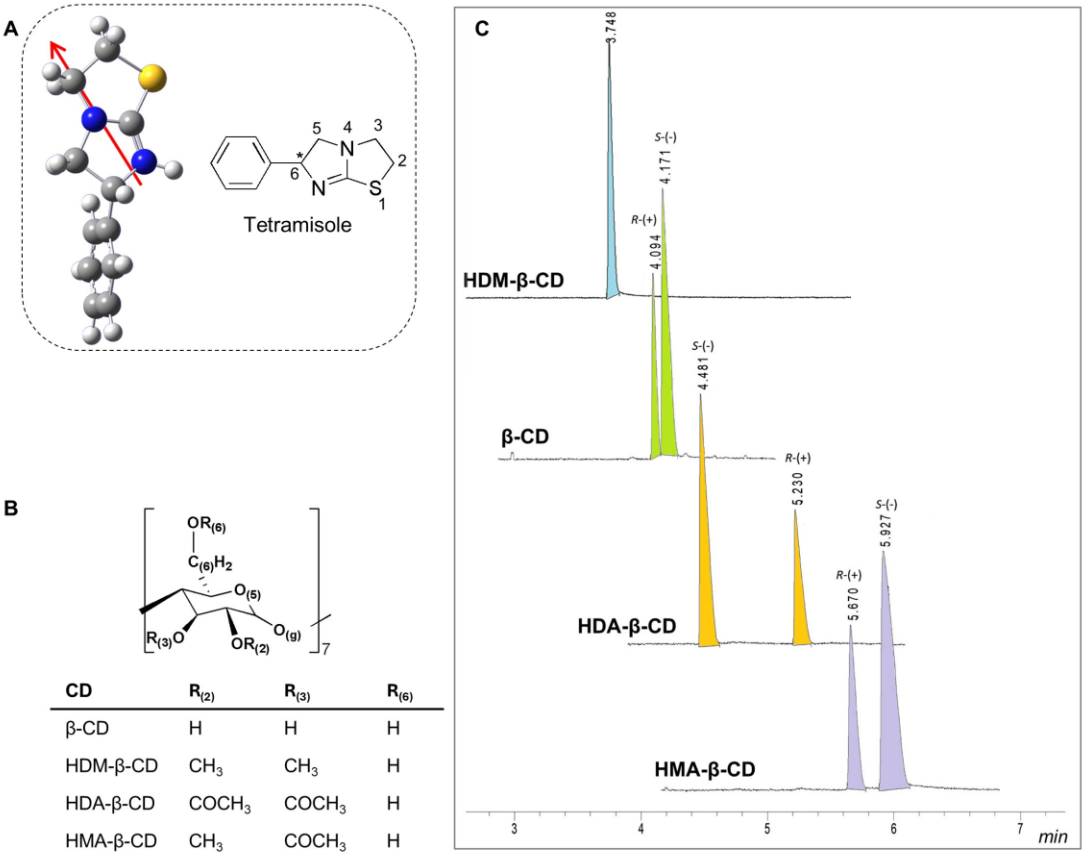

CD	$R_{(2)}$	$R_{(3)}$	$R_{(6)}$
β-CD	H	H	H
HDM-β-CD	CH_3	CH_3	H
HDA-β-CD	$COCH_3$	$COCH_3$	H
HMA-β-CD	CH_3	$COCH_3$	H

Figure 1. (A) Structures of tetramisole (drawing) and its protonated (*R*)-enantiomer (three-dimensional model; color legend: grey, carbon; pale grey, hydrogen; blue, nitrogen; yellow, sulphur; the calculated dipole moment vector is shown as a red arrow). (B) Substitution patterns of β-CD, HDM-β-CD, HDA-β-CD and HMA-β-CD. The structures of the CDs are symbolized by the $^4C_1$ chair conformation of the D-glucopyranose moiety and numbering/notation of the atoms refers to the description of the respective atoms in the text. (C) Electropherograms of the CE separation of a spiked tetramisole sample with [(*S*)/(*R*) = 2/1] in the presence of HDM-β-CD, β-CD, HDA-β-CD and HMA-β-CD. Experimental conditions: 24.5/32 cm, 50 µm I.D. fused-silica capillary; 100 mM phosphoric acid buffer adjusted to pH 3.0 with TEA. 20 °C; 15 kV; [CD] 17.6 mM.

These enantioseparation systems and related outcomes were used as benchmark experimental data to evaluate the efficacy of combining NMR Rotating-Frame Overhauser Enhancement Spectroscopy (ROESY) analyses and quantum mechanics (QM)-based computations to derive reliable information about enantiomer binding and recognition mechanisms. In other words, we aimed at evaluating the efficacy of this approach to properly model the experimental system.

The arguments for using CDs as chiral selectors in mechanistic studies have been highlighted in several studies and reviews (Chankvetadze & Scriba, 2023; Peluso & Chankvetadze, 2021; Peluso & Chankvetadze, 2022). Tetramisole was used as analyte because of its structural features, which make the compound and the CD-complexes suitable as test probes for modeling studies. Tetramisole is small enough to avoid steric hindrance to dominate and control the inclusion process. Moreover, tetramisole is a molecule with limited degrees of freedom so that the computation of too many conformers of the analyte is not required.

The hypothesis of this study was if the factors controlling analyte-CD interaction could be identified and quantified by using CE, NMR spectroscopy and QM-based computations as complementary techniques. Specifically, we hypothesized that a different balance between the noncovalent interactions acting in the analytical systems under investigation is responsible for the different experimental outcomes obtained by using derivatized β-CDs compared to native β-CD.

2 Computations

The tetramisole structures were treated as fully protonated in accord with the experimental parameter pH = 3.0 used in CE analyses. The 3D structure of β-CD was released from Cambridge Structural Database (CSD) (Thomas et al., 2010), entry AGAZOX (Alexander et al., 2002). HDM-β-CD, HDA-β-CD and HMA-β-CD were built using the DFT optimized β-CD structure as a template and changing the proper hydroxy hydrogen atoms bound to the $O_{(2)}n$ and $O_{(3)}n$ atoms ($1 \leq n \leq 7$) to methyl and/or acetyl groups. In Figure 1B, labels and numbering of the atoms of a D-glucopyranose unit in the typical $^4C_1$ chair conformation are shown. The tetramisole enantiomers and all β-CDs used in this study were optimized at DFT level using Gaussian 16W (Gaussian 16, 2016), with the B3LYP functional and the 6-31G(d) as basis sets, applying tight convergence criteria. The optimization procedures were performed in the gas phase, using the solvation model based on density (SMD) (water) variation of IEFPCM (integral equation formalism for polarizable continuum model) of Truhlar and co-workers (Marenich et al., 2009), with and without dispersion correction using the D3 version of Grimme's dispersion with Becke-Johnson damping (*gd3bj*) (Grimme et al., 2011). Complete computational results and coordinates of the optimized CD structures (SMD, water) are reported in the Supporting Information. Energies are reported in Hartree or kcal·mol^{-1} (1 Hartree = 627.503 kcal·mol^{-1}), dipole moments in Debye, polarizability in au (atomic unit, electrons/Bohr) and quadrupole moment XX, YY, and ZZ components (Q_{xx}, Q_{yy}, Q_{zz}) in Debye-Å. Electrostatic potential (V) maxima and minima mapped on the molecular electron density isosurfaces ($V_{S,max}$ and $V_{S,min}$) (au) were calculated using Gaussian 16W. The electrostatic potential in a point **r**, $V(\mathbf{r})$, is given by Eq. (1):

$$V(\mathbf{r}) = \sum_A \frac{Z_A}{R_A - r} - \int \frac{\rho(r)dr'}{|r' - r|} \quad (1)$$

where Z_A is the charge on nucleus A located at R_A, and $\rho(\mathbf{r})$ is the electron density function. (*R*)- and (*S*)-Tetramisole/CD complexes were generated by manually docking the analyte into the CD cavity at different degrees of penetration obtaining between 4 and 8 complexes for each CD/enantiomer complex. Subsequently, the structure of each complex was optimized at DFT level (B3LYP/6-31G(d,p)) applying the SMD (water) solvation model. For the lowest-energy complex, geometry optimization was also performed with the *gd3* dispersion correction (Grimme et al., 2010). For the lowest-energy complexes, binding energies, $E_{binding}$, and differences in binding energies of the complexes, $\Delta E_{binding}$, were computed based on the following equations:

$$E_{binding} = E_{complex} - E_{tetramisole} - E_{CD} \quad (2)$$

$$\Delta E_{binding} = E_{binding\ (2nd\ eluted\ enantiomer)/CD\text{-}complex} - E_{binding\ (1st\ eluted\ enantiomer)\text{-}complex} \quad (3)$$

For the CDs and the tetramisole/CD complexes, the solvation free energy was calculated as the difference between energy quantities calculated in the SMD environment and in gas phase based on equation (4):

$$G_{solvation} = G_{SMD} - G_{gas\ phase} \quad (4)$$

Other detailed information is reported in the Supporting Information.

3 Experimental

3.1 Materials

Racemic tetramisole hydrochloride ((±)-2,3,5,6-tetrahydro-6-phenylimidazo[2,1-b]thiazol hydrochloride) and (S)-(−)-tetramisole hydrochloride, β-CD ($C_{42}H_{70}O_{35}$, Mr 1134.98, HPLC purity > 97%) were supplied by Sigma-Aldrich Merck (Darmstadt, Germany). *Heptakis*(2,3-di-*O*-acetyl)-β-CD (HDA-β-CD) ($C_{70}H_{98}O_{49}$, Mr 1723.50), *heptakis*(2,3-di-*O*-methyl)-β-CD (HDM-β-CD) ($C_{56}H_{98}O_{35}$, Mr 1331.36) and *heptakis*(2-*O*-methyl-3-*O*-acetyl)-β-CD (HMA-β-CD) ($C_{63}H_{98}O_{42}$, Mr 1527.43) (all with HPLC purity > 97%) were provided by Dr. M. Malanga from CarboHyde (Budapest, Hungary). Other details are reported in Supporting Information.

3.2 Capillary electrophoresis

All CE experiments were carried out on a capillary electrophoresis system Agilent G1600 (Agilent Technologies, Waldbronn, Germany) equipped with an autosampler, an on-capillary diode-array detector and air-based temperature control system. The Chemstation B.04.03 software from Agilent Technologies was used for instrument control and data analysis. Other details are reported in Supporting Information.

3.3 NMR spectroscopy

NMR spectra were recorded on a Varian NMR System (Varian Inc., Palo Alto, CA, USA), equipped with a CHX $^{1}H/^{13}C/^{15}N–^{31}P$ probe head, a z-gradient module and a variable temperature unit. Detailed information about NMR experiments is reported in Supporting Information.

4 Results and Discussion

The first aim of the present study was to examine the effect of modifications of CD-macrocycle on the affinity strength and affinity pattern of tetramisole enantiomers toward the four CDs used as chiral selectors. CE is the best technique for collecting this type of information given its high separation efficiency. Indeed, in CE thermodynamic selectivity of enantiorecognition in the range of 1.01 is sufficient to observe baseline enantioseparations (Chankvetadze, 2004, Chankvetadze, 2018). Thus, CE is suitable to study fine variations in the enantiodifferentiation power of chiral selectors and in the affinity strength and pattern of the selectand-enantiomer toward the selector by evaluating the separation factor α and migration times, respectively. Furthermore, CE offers a unique opportunity to produce benchmark experimental data to validate related theoretical models. By using different CDs as chiral selectors with the same molar concentration, the migration time of enantiomers will provide approximate information on the binding strength within the CD-selectand complexes. In this regard, it is worth mentioning that using different CDs in the background electrolyte, even at the same molar concentrations, may impact the viscosity of the medium in different ways and, consequently, the migration times of the selectands. However, when the experiment is performed under permanent voltage conditions, the effect of the viscosity on the migration time of selectand can be estimated and corrected based on the change of the electric current generated in the capillary. Alternatively, relative viscosity of a background electrolyte can be measured with CE-instrument and used for the correction of migration times.

Thus, using selected outcomes derived from CE analyses, ROESY experiments and QM calculations were used to examine if there was any significant difference in the structure of selector-selectand complexes that could be responsible for the changes of the affinity strength and affinity patterns between selector and selectand observed in CE. Based on this approach, the structures of the β-CDs and of the tetramisole-enantiomer/CD complexes were modeled by applying electronic structure methods in the QM domain with the aim to compute and identify the forces responsible for selector-selectand binding and for enantioselective recognition in selector-selectand complexes. A second goal of the computational study was to evaluate the capability and accuracy of the used model chemistry to describe correctly the experimental systems. It is worth stressing that ROESY and QM analyses were performed, and the results compared, to derive a model of the “real” system in an orthogonal perspective aiming at the mutual validation of data based on theoretical principles and experimental data produced using a different independent method to describe the same system. Thus, information derived from the ROESY analysis of the complex structures was not used to set up the input structures for the modeling calculations.

4.1 Capillary electrophoresis enantioseparation of tetramisole enantiomers

Among the four studied β-CDs, the solubility of native β-CD in the aqueous buffer is the lowest. Therefore, in CE experiments, β-CD was dissolved at its maximum concentration of 20 $mg \cdot ml^{-1}$ (17.6 mM). The other three β-CD derivatives were also used at the same molar concentration. The results of these experiments are shown in Figure 1C and data are summarized in Table S1 (supporting information).

The following conclusions can be drawn from these results:

1) The affinity of the tetramisole enantiomers toward β-CD is reduced by methylation of the hydroxyl groups at the 2- and 3-positions on the wider rim of the macrocycle. In contrast, an increase of the affinity of the tetramisole enantiomers toward the selector was observed for the acetylated derivatives compared to native β-CD. Based on the migration times, the affinity increase was highest for HMA-β-CD indicating that the presence of both methyl and acetyl substituents at the wider rim of the β-CD had an apparent synergistic but not an additive effect on the selectand-CD affinity strength. The non-additivity seems also logical because HMA-β-CD is a new recognition system and not a hybrid between HDM-β-CD and HDA-β-CD.

2) The separation factor α with HDA-β-CD was significantly higher (α = 1.17) compared to the other CDs (1.00 ≤ α ≤ 1.05) under the applied experimental conditions indicating that acetylation significantly improved the enantiomer differentiation power of β-CD (α = 1.02). This is in good correlation with previous observations made by our research group (Chankvetadze et al., 2003). Whereas the affinity of tetramisole enantiomers was highest for HMA-β-CD compared to HDA-β-CD, enantiorecognition selectivity for HMA-β-CD (α = 1.05) was lower compared to that of HDA-β-CD but higher than that of β-CD. In contrast to acetylation, methylation of β-CD at the same positions drastically reduced not only selectand affinity toward the chiral selector, but also its enantiomer recognition ability. Thus, HDM-β-CD was able to separate the enantiomers of tetramisole only at a concentration as high as 112.7 mM (α = 1.02) (Figure S1, supporting information).

3) Interesting observations could be also made in terms of the affinity patterns of the tetramisole enantiomers toward the CDs. Acetylation or methylation at both 2- and 3-positions [EMO = (*S*) > (*R*)] reversed the affinity pattern of tetramisole compared to native β-CD [EMO = (*R*) > (*S*)] (Figure 1C and S1, supporting information). However, 2-methylation and 3-acetylation did not affect the EMO and (*R*) > (*S*) was observed as in the case of β-CD as chiral selector. This observation underlines that the interplay of noncovalent forces involved in enantioselective recognition with CDs is very complex. If the introduction of acetyl or methyl moieties into the structure of β-CD at the 2- and 3-positions simultaneously induced the affinity reversal of the tetramisole enantiomers toward the selectors compared to native β-CD, one might assume that this would also apply to a “mixed” β-CD derivative, i.e. methylation a position 2 and acetylation at position 3 (HMA-β-CD). However, this was not the case.

4.2 NMR spectroscopy

Since the most drastic difference in the enantioselective recognition properties (significant increase of enantiomer discrimination ability and reversal of the enantiomer affinity pattern) was observed for acetylation at the 2- and 3-positions, β-CD and HDA-β-CD were selected for detailed NMR spectroscopic studies. Splitting of most diastereotopic proton signals was observed due to complexation induced chemical shift (CICS) difference between the two enantiomers of racemic tetramisole in the presence of both CDs. Only the results for H-6 protons in case of both CDs are shown in Figure 2.

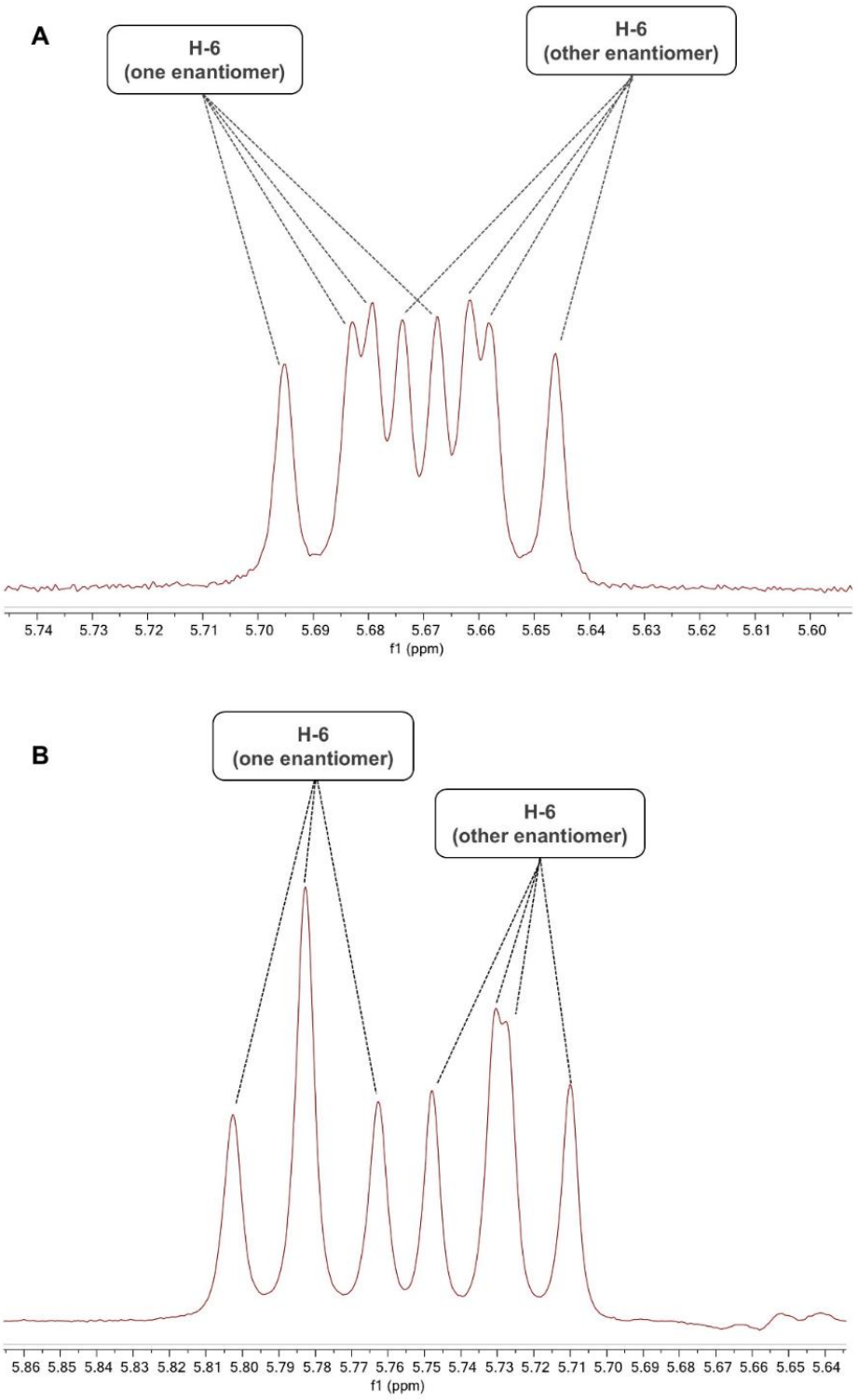

Figure 2. Expanded partial NMR spectra showing the signals of tetramisole H-6 of the complexes of racemic tetramisole with (A) β-CD and (B) HDA-β-CD. Experimental conditions: 500 MHz, 25°C; sample A: 1.5 mg tetramisole and 14.0 mg β-CD in 0.7 mL 100 mM D_3PO_4 buffer (pH 3.0, TEA); sample B: 1.6 mg tetramisole and 14.7 mg HDA-β-CD in 0.6 mL 100 mM D_3PO_4 buffer (pH 3.0, TEA).

By comparing the signal splitting for the H-6 proton (bound to the chiral center) one can see a good correlation between CE and NMR spectroscopic results with regard to the chiral recognition ability of both CDs. As shown in Figure 1C, HDA-β-CD is a significantly better chiral selector compared to native β-CD. Much stronger CICS was observed between the H-6 diastereotopic protons in the presence of HDA-β-CD (0.055 ppm) (Figure 2B) compared β-CD (0.028 ppm) (Figure 2A). An even more significant difference between the ^{1}H NMR spectra of β-CD and HDA-β-CD complexes was also observed. In the spectrum of the (*R*,*S*)-tetramisole/β-CD complex, for each enantiomer, the signal of the H-6 proton appeared as a doublet of doublets evidencing the nonequivalence of the two H-5 protons in both enantiomers. On the contrary, in the spectrum of the (*R*,*S*)-tetramisole/HDA-β-CD complex, the signal of the H-6 proton of the (*S*)-tetramisole (levamisole) appeared as a triplet, showing the equivalence of the two H-5 protons, whereas for the (*R*)-enantiomer the signal of the H-6 proton appeared as a doublet of doublets confirming the nonequivalence of the H-5 protons in this enantiomer.

Based on ROESY data collected by selective irradiation experiments of protons of the CDs and racemic tetramisole, the most likely tentative structures of the complexes were derived as shown in Figure 3. Although there is no doubt that ROESY experiment in NMR spectroscopy is a powerful technique for deriving tentative structures of selector-selectand complexes in solution based on the spatial proximity of protons (Salgado & Chankvetadze, 2016), actual (true) structures cannot be concluded and still leave room for (personal) interpretation. Moreover, ROESY did not provide any clear indication to explain why the acetylation of the 2- and 3-hydroxyl groups at the secondary rim of β-CD so dramatically changed the enantioselective recognition ability and pattern of HDA-β-CD compared to β-CD.

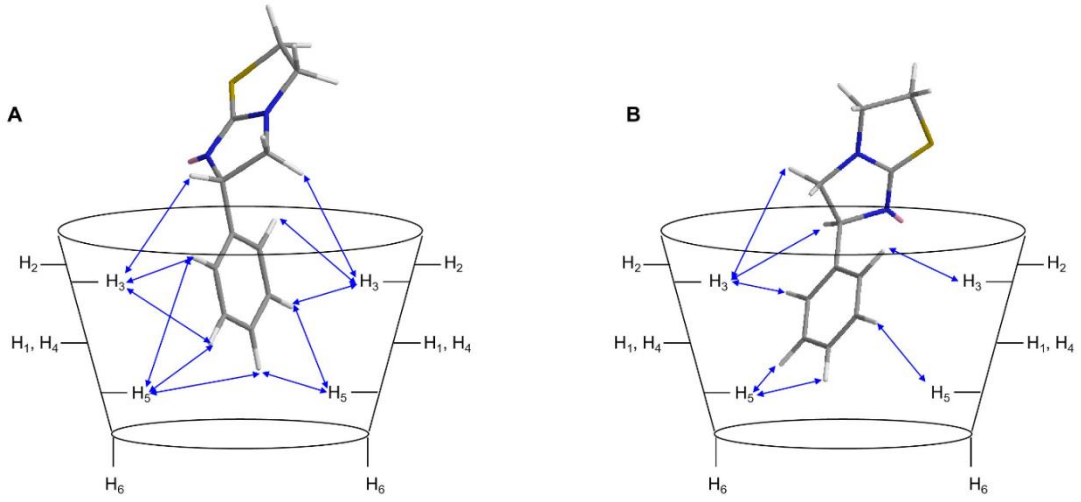

Figure 3. Schematic representation of the complexes formed between tetramisole and (A) β-CD and (B) HDA-β-CD. The intermolecular NOEs deduced from ROESY experiments are indicated by blue arrows.

4.3 Molecular modeling study on the complexation of tetramisole enantiomers by β-CDs

The establishment of enantioselective interactions between the enantiomers of a chiral analyte and the chiral selector in the background electrolyte is the prerequisite for obtaining an enantioseparation in CE (Chankvetadze & Blaschke, 2001; Chankvetadze, 2018). The enantioselective interactions can be

reflected in different binding constants of the two enantiomers with a chiral selector, in different mobilities of the transient diastereomeric complexes or in both (Chankvetadze, 1997; Chankvetadze, 2018). It is worth mentioning that the affinity pattern of enantiomers toward studied CDs was considered to be solely responsible for the observed enantiomer migration order (EMO) in the present study. Based on the structure of studied analyte and CDs this assumption was justified. Thus, the complexation of the tetramisole enantiomers by β-CD, HDM-β-CD, HDA-β-CD, and HMA-β-CD contributed to determine the enantioseparations in CE. With the aim of exploring and comparing the molecular bases of these complexation processes, the computational study was performed with three specific purposes:

1) To inspect in depth the impact of the derivatization at the wider rim of the macrocycles, identifying molecular properties and structural features which may be considered as pre-requisites to obtain successful enantioseparations of tetramisole.
2) To elucidate noncovalent interactions underlying the complexation processes of the tetramisole enantiomers by the β-CD derivatives.
3) To use the CE experimental data as benchmark to evaluate the efficacy of the selected computational methods to describe binding and enantioselective recognition phenomena in terms of electronic energies, highlighting possible pitfalls and failures of the methods to correctly describe the experimental results. As already mentioned above, developing computational methods as accurate and reliable as possible to properly account for very subtle differences in the experimental results observed in enantioseparation science is rather challenging. For instance, based on the experiments summarized in Figure 1C, a virtual model of the set of CE enantioseparations should be able to account for fine differences *a*) in a range of about 2.2 min for the migration times of the tetramisole enantiomers as a result of the complexation of each enantiomer with the four β-CDs (eight complexes), and *b*) in the tight range of $1.02 \leq \alpha \leq 1.17$ ($\Delta\alpha = 0.15$) for the enantioselectivity values corresponding to very low free energy differences calculated based on the equation $\Delta\Delta G = -RT\ln\alpha$ in the range $11.7 \leq \Delta G \leq 93.0$. ($cal \cdot mol^{-1}$). Thus, the derived model should be consistent with the experimental system(s) in terms of EMOs, binding energies and binding energy differences ($\Delta E_{binding}$) for each pair of transient diastereomeric enantiomer/CD complexes. These should correlate properly with the affinity patterns of selectand to the chiral selector, migration times and separation factors, respectively.
4) To compare computational and ROESY results and evaluate the agreement of the tetramisole-CD complexation models derived from the two techniques independently of each other.

4.3.1 Computed optimized structures of native and derivatized β-CDs by quantum mechanics

The results obtained in the CE enantioseparation of tetramisole with native β-CD and the three single isomer 2,3-disubstituted-β-CDs (Figure 1C) indicated that derivatization of β-CD by introducing methyl and/or acetyl groups at the wider rim impacts on the enantiorecognition ability of the macrocycles. Furthermore, derivatization also improves the solubility of the native macrocycle in water (Fejős et al., 2020) and thus, indirectly its binding and enantioselective recognition ability. The main direct effect of substituting the hydroxyl hydrogen atoms at the wider rim results in the disruption of the HB network sustaining the round shape of β-CD. This has an impact on the size, shape and flexibility of the CD

cavity, which are essential elements determining the features of the complexation process (Peluso et al., 2024; Perez-Miron et al., 2008).

To address these issues, the structures of the four CDs were optimized by QM (Tables S2-S27, supporting information). The DFT optimized structures of β-CD and the three derivatives calculated by using the implicit SMD solvation (water) to account for the experimental aqueous environment were compared with the aim to evaluate the impact of derivatization on CD topography and on the stereoelectronic properties of the macrocycles

The computed β-CD structure featured a regular shape sustained by inter-residue intramolecular $O_{(3)}nH\cdots O_{(2)}n'$ HBs (average H···O length = 1.864 ± 0.004 Å, average O-H···O angle = 161.933° ± 0.444) and weaker intra-residue intramolecular $O_{(6)}nH\cdots O_{(5)}n$ HBs (average H···O length = 2.424 ± 0008 Å, average O-H···O angle = 104.747 ± 0.414) occurring at the wider and the narrower rim, respectively. Given this HB pattern as reference for comparison, intramolecular HB patterns and geometric parameters of the DFT optimized structures of the three derivatized β-CDs were compared to determine the impact of the methyl and/or the acetyl group(s) on the shape of the macrocycle.

Table 1. Average distances [Å] and angles [°, degree] including the related standard deviations of intramolecular HBs at the wider [inter-residue $O_{(3)}nH\cdots O_{(2)}n'$] and at the narrower [intra-residue $O_{(6)}nH\cdots O_{(5)}n$] rim, and distance between opposite glycosidic oxygen atoms [$O_{(g)}n\cdots O_{(g)}n'$] and between opposite $C_{(6)}$ atoms (narrower rim) [$C_{(6)}n\cdots C_{(6)}n'$] ($\Delta R_{l\text{-}s}$) [Å] ($1 \le n \le 7$), measured for DFT optimized β-CD, HDM-β-CD, HMA-β-CD, and HDA-β-CD structures [B3LYP/6-31G(d); SMD, water] using the Chimera version 1.16 program.

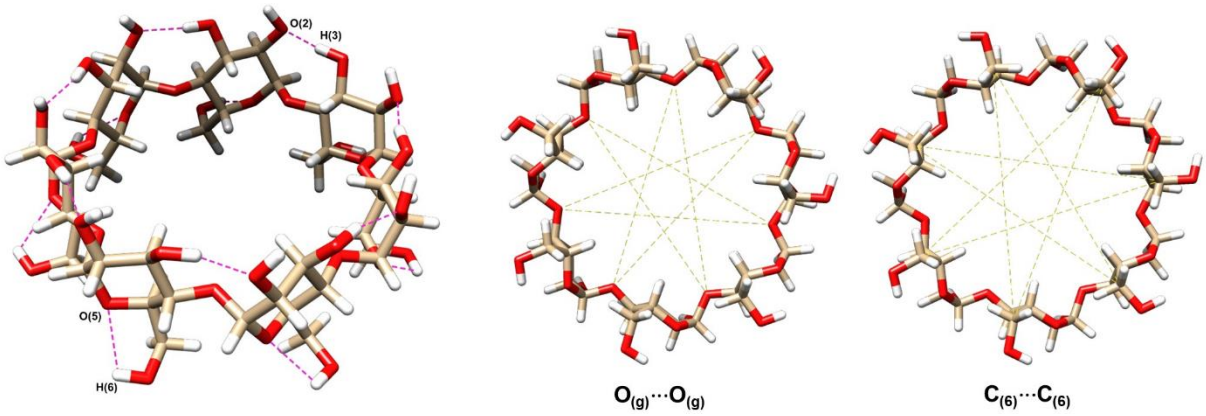

Parameter	β-CD	HDM-β-CD	HMA-β-CD	HDA-β-CD
$O_{(3)}nH\cdots O_{(2)}n'$ distance	1.864 ± 0.004			
$O_{(3)}n\text{-}H\cdots O_{(2)}n'$ angle	161.933 ± 0.444			
$O_{(6)}nH\cdots O_{(5)}n$ distance	2.424 ± 0.008	2.452 ± 0.056	2.478 ± 0.055	2.486 ± 0.044
$O_{(6)}n\text{-}H\cdots O_{(5)}n$ angle	104.747 ± 0.414	104.140 ± 1.472	103.342 ± 1.291	102.935 ± 1.208
$O_{(g)}n\cdots O_{(g)}n'$ $\Delta R_{l\text{-}s}$	0.023	1.196	1.106	1.164
$C_{(6)}n\cdots C_{(6)}n'$ $\Delta R_{l\text{-}s}$	0.312	3.940	4.053	4.559

The average lengths and angles (with related standard deviations) associated with the intramolecular HBs of the CD macrocycles are reported in Table 1. The strength of the HBs is considered to increase as the H···O distance, typically in the range 1.5–2.4 Å, decreases. Furthermore, given the O-H···O angle as a measure of the deviation of the HB directionality from the ideal reference angle of 180°, the strength

of the HB increases as the O-H···O angle tends to the reference value. Given that introduction of the 2,3-substituents disrupts the HB network compared to β-CD at the wider rim, a clockwise HB pattern at the narrower rim could be only observed. As a result, the 2,3-disubstituted β-CDs showed higher flexibility due to the increased steric hindrance at the wider rim and a weakening of the HB strength at the narrower rim compared to β-CD. Indeed, the derivatization at the wider rim may impact the HBs at the narrower rim in the following two ways (Peluso et al., 2024): *a*) when the derivatization at the wider rim preserves the HB network, like in the case of *heptakis*(2-*O*-methyl)-β-CD, the HBs at the narrower rim become stronger due to the compression effect induced by this derivatization; *b*) when the derivatization at the wider rim disrupts the HB network at this rim, the HBs at the narrower rim become weaker as a result of the steric compression of the overall system and also due to the higher flexibility of the glycosyl bonds that are not constrained by the HBs at the wider rim. Accordingly, for all derivatized macrocycles, the average length and angle of these HBs increased and decreased, respectively, with a higher variability compared to native β-CD. On this basis, the strength of the HB network at the primary rim decreased following the order β-CD > HDM-β-CD (+ 0.028 Å, - 0.607°) > HMA-β-CD (+ 0.054 Å, - 1.405°) > HDA-β-CD (+ 0.062 Å, - 1.812°).

To also evaluate the extent of cavity distortion induced by derivatization at the 2- and 3-positions compared to the round-shaped β-CD, we derived the $\Delta R_{l\text{-}s}$ value as the calculated difference between the longest and the shortest $O_{(g)}\cdots O_{(g)}$ and $C_{(6)}\cdots C_{(6)}$ distances from the seven pairs of opposite glycosidic oxygen and methylene carbon atoms of the CD (Li et al., 2012). A small value of $\Delta R_{l\text{-}s}$ indicated that the cavity shape was round, whereas a high value revealed an elliptically distorted cavity. The derivatized CDs showed higher $\Delta R_{l\text{-}s}$ values, ranging from 1.106 to 1.196 Å [$O_{(g)}\cdots O_{(g)}$] and from 3.940 to 4.559 Å [$C_{(6)}\cdots C_{(6)}$], compared to the round-shaped β-CD showing values of 0.023 Å and 0.312 Å, respectively. Thus, the 2,3-disubstituted β-CDs featured a less round-shaped cavity, or a higher tendency to an elliptic shape, compared to the native macrocycle. In particular, the distortion of the narrower rim, in terms of $C_{(6)}\cdots C_{(6)}$ $\Delta R_{l\text{-}s}$, again followed the order β-CD > HDM-β-CD (+ 3.628 Å) > HMA-β-CD (+ 3.741 Å) > HDA-β-CD (+ 4.247 Å).

The structures of β-CD, HDM-β-CD, HMA-β-CD and HDA-β-CD in the gas phase were also computed (Table 2) to evaluate the impact of the implicit solvation on the CD conformation and related geometric parameters. For all CDs, solvation weakened the HBs at the narrower rim compared to the corresponding HBs computed in gas phase. Although the $\Delta R_{l\text{-}s}$ slightly increased for β-CD due to the implicit solvation [$\Delta R_{l\text{-}s}$: $O_{(g)}\cdots O_{(g)}$ 0.006 Å (gp) vs. 0.023 Å (SMD); $C_{(6)}\cdots C_{(6)}$ 0.013 Å (gp) vs. 0.312 Å (SMD)], the cavity of the solvated β-CD maintained a round shape. In contrast, for all derivatized β-CDs, reduced values of $\Delta R_{l\text{-}s}$ related to $O_{(g)}\cdots O_{(g)}$ and $C_{(6)}\cdots C_{(6)}$ distances were obtained in most cases using the SMD solvation. This resulted in more round shapes of the solvated derivatized β-CDs compared to the structures computed in the gas phase, with the availability of larger cavities for the complexation of guests (Figure 4). This confirms how much it is wrong to model CD inclusion complexes in the vacuum, neglecting the essential role of the medium.

Table 2. Average distances [Å] and angles [°, degree] including the related standard deviations of intramolecular HBs at the wider [inter-residue $O_{(3)}nH\cdots O_{(2)}n'$] and at the narrower [intra-residue $O_{(6)}nH\cdots O_{(5)}n$] rim, and distance between opposite glycosidic oxygen atoms [$O_{(g)}n\cdots O_{(g)}n'$] and between opposite $C_{(6)}$ atoms (narrower rim) [$C_{(6)}n\cdots C_{(6)}n'$] ($\Delta R_{l\text{-}s}$) [Å] ($1 \leq n \leq 7$), measured for DFT optimized β-CD, HDM-β-CD, HMA-β-CD, and HDA-β-CD structures [B3LYP/6-31G(d); gas phase] using the Chimera version 1.16 program.

Parameter	β-CD	HDM-β-CD	HMA-β-CD	HDA-β-CD
$O_{(3)}nH\cdots O_{(2)}n'$ distance	1.879 ± 0.001			
$O_{(3)}n\text{-}H\cdots O_{(2)}n'$ angle	164.456 ± 0.041			
$O_{(6)}nH\cdots O_{(5)}n$ distance	2.324 ± 0.001	2.368 ± 0.055	2.389 ± 0.035	2.445 ± 0.117
$O_{(6)}n\text{-}H\cdots O_{(5)}n$ angle	106.736 ± 0.040	106.406 ± 1.019	104.879 ± 0.715	103.549 ± 1.948
$O_{(g)}n\cdots O_{(g)}n'$ $\Delta R_{l\text{-}s}$	0.006	1.948	1.181	1.839
$C_{(6)}n\cdots C_{(6)}n'$ $\Delta R_{l\text{-}s}$	0.013	8.125	5.135	4.462

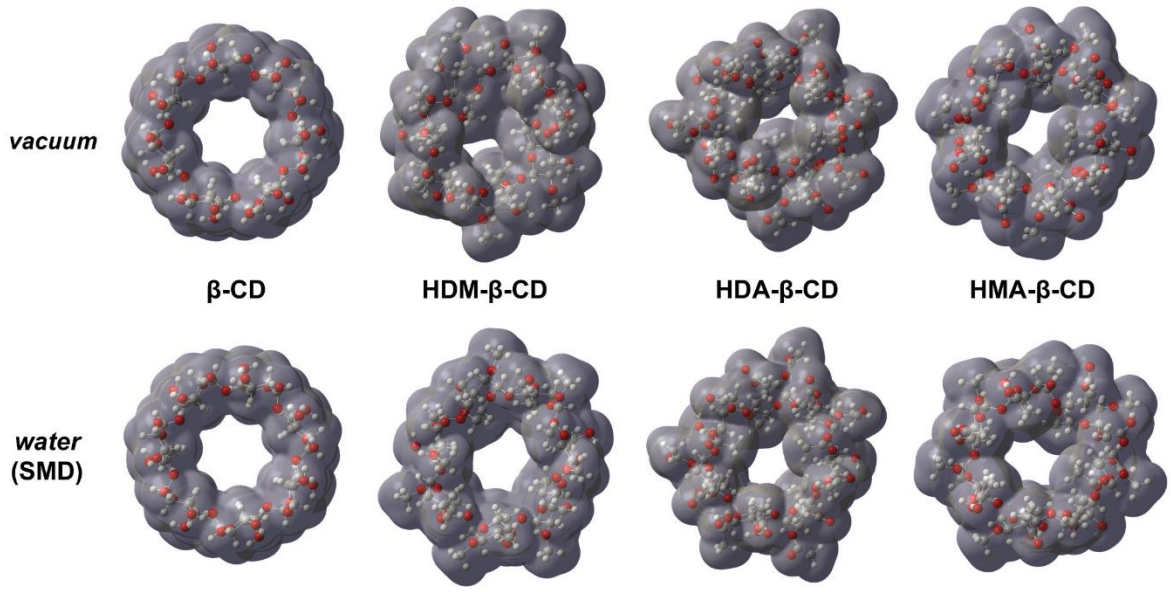

Figure 4. Electron density isosurfaces (isovalue 0.001 au) (viewpoint on the wider rim) of native β-CD and single isomer HDM-β-CD, HDA-β-CD and HMA-β-CD calculated at DFT level of theory [B3LYP/6-31G(d)] in the gas phase and with the SMD solvation model (water). Colour legend: carbon, grey; hydrogen, white; oxygen, red.

On the other hand, the introduction of substituents in the native macrocycle increases the ability of the corresponding CD to interact with the surrounding water molecules because of the disruption of the HB network within β-CD (Saokham et al., 2018). In partial agreement with this observation, the calculated solvation free energy ($\Delta G_{solvation}$) increased in the order HDM-β-CD (-74.44 kcal·mol^{-1}) < β-CD (-84.80 kcal·mol^{-1}) < HMA-β-CD (-97.01 kcal·mol^{-1}) < HDA-β-CD (-114.01 kcal·mol^{-1}) (Table 3 and Tables S26 and S27, supporting information). The higher solubility of HDM-β-CD compared to β-CD and a lower solvation free energy was determined for the dimethylated derivative. This apparent inconsistency is not surprising considering that implicit solvation models may be unsuitable to describe complex phenomena like the anomalous solubility of β-CD, which cannot be explained by its free energy of

solvation/hydration alone (Cai et al., 2008; Coleman et al., 1992). The same incongruence was also observed by applying IEFPCM as solvation model.

The size of the isosurface area, the dipole moment, polarizability, the zero-point vibrational energy (ZPVE), the standard deviation of the quadrupole components [*Q* SD (±)], and the contribution of the dispersion energy to the total energy (E_{disp}) were also computed for the β-CD derivatives as summarized in Table 3. β-CD was not included in this comparison as only molecular properties of structures with homogeneous topography like the three 2,3-disubstituted CDs were compared. Indeed, β-CD presented a different topography with both rims decorated and constrained by HB networks. On this basis, the following observations can be highlighted:

Table 3. Isosurface area [Å^2], dipole moment [Debye], polarizability [au], zero-point vibrational energy (ZPVE) [kcal·mol^{-1}], standard deviation of quadrupole moment components (*Q* SD) [Debye-Å], dispersion energy contribution to the total electronic energy ($E_{disp.}$, *gd3bj* correction) [kcal·mol^{-1}], and solvation free energy ($\Delta G_{solvation}$) [kcal·mol^{-1}] calculated for the DFT optimized β-CD, HDM-β-CD, HMA-β-CD, and HDA-β-CD structures [B3LYP/6-31G(d); SMD, water].

Molecular properties	β-CD	HDM-β-CD	HMA-β-CD	HDA-β-CD
Isosurface Area	908.52	1133.18	1209.13	1351.80
Dipole moment	1.48	5.81	16.80	16.74
Polarizability	747.82	954.97	1069.99	1180.65
ZPVE	761.76	1010.74	1054.09	1096.18
Q SD (±)	2.30	11.41	34.00	74.29
E_{disp}	-205.39	-260.91	-300.01	-328.91
$\Delta G_{solvation}$	-84.80	-70.44	-97.01	-114.01

1) *Isosurface area*. The electron density isosurface represents the molecular area of contact available for the interaction of the CD with the analyte. The nature of the noncovalent interactions underlying analyte-CD contact depends on the electron charge density distribution on CD and analyte isosurfaces (Figures 5 and 6). On this basis, a higher isosurface area could enhance analyte-CD contacts. This could correlate with analyte-CD binding affinity, but not necessarily with binding selectivity.
2) *Dipole moment*, *polarizability*, and *quadrupole moment components*. These molecular properties provide information about the asymmetry degree (*dipole moment*), the capability to be distorted in the presence of an external field (*polarizability*), and the shape (*quadrupole moment*) of the electron charge distribution of the CD (Hickey & Rowley, 2014; Vijayakumar & Kolandaivel, 2006). The acetylated CDs showed higher dipole moments and vectors with opposite directions compared to β-CD and HDM-β-CD (Figure 5). These CDs also showed higher polarizability values indicating higher mobility of the electrons within these macrocycles. Whereas equal XX, YY, and ZZ quadrupole moment (*Q*) components indicate a spherical total electron distribution, the presence of one component larger than the others indicates an elongation of the electron cloud along that axis. On this basis, given the average value of the three components, the extent of the related standard deviation (*Q* SD) tells us about the shape of the electron distribution cloud. Again, higher *Q* SD values were determined for the acetylated

CDs, indicating the presence of a distorted non spherical distribution of the electron charge density.

3) *Zero-point vibrational energy* and c*ontribution of dispersion to the total energy*. The ZPVE is an estimation of the energy of the molecule in its lowest vibrational state at 0 K, in the absence of translational and rotational energy. Thus, this value of energy correlates with the oscillation ability of the atoms in a molecule, which in turn is considered to correlate with the dispersion ability of a molecule (London, 1937). Accordingly, the computed dispersion contribution to the total energy ($E_{disp.}$) of the studied CDs increased as the ZPVE values, and again the acetylated CDs showed the highest values of these computed descriptors.

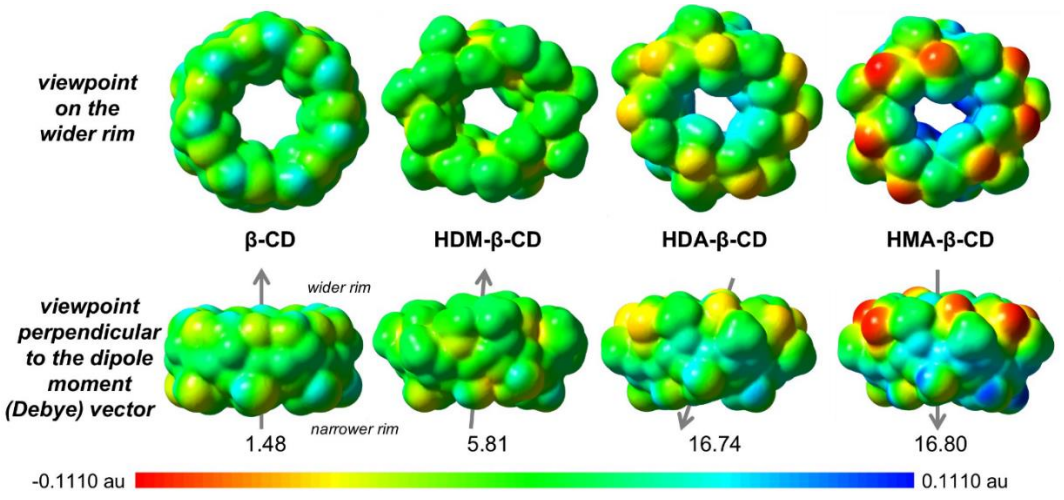

Figure 5. Electrostatic potential values mapped on density isosurfaces (isovalue 0.001 au) of β-CD and the single isomer HDM-β-CD, HDA-β-CD and HMA-β-CD calculated at DFT level of theory [B3LYP/6-31G(d); SMD, water] (for numerical values see Tables S5, S9, S17, and S25, supporting information,).

Thus, not only geometric parameters associated with the optimized CD conformation, but also the stereoelectronic properties of the macrocycles affected the enantioseparation mechanisms. To obtain further insight into this issue, we also calculated and compared the *V* extrema of pivotal atoms of the macrocycles potentially functioning as HB acceptors [$O_{(g)}$, $O_{(5)}$, $O_{(2)}$, $O_{(3)}$, $O_{(6)}$, C=$\underline{O}_{(2)}$, C=$\underline{O}_{(3)}$], in general (but not always) featuring negative values of $V_{S,min}$ (nucleophilic sites), and HB donor [O$\underline{H}_{(6)}$] featuring positive values of $V_{S,max}$ (electrophilic sites). Regarding the *V* fingerprints of the four CDs depicted in Figure 6, the following conclusions could be drawn:

1) Two types of *V* patterns were identified. The first is related to β-CD and HDM-β-CD providing lower selectivity values, while the second refers to the acetylated β-CDs showing better selectivity in the CE enantioseparation of tetramisole.
2) The main difference concerned the $O_{(g)}$, $O_{(5)}$, and $O_{(2)}$ sites that present reduced electron charge density with positive $V_{S,min}$ values in the acetylated β-CDs compared to β-CD and HDM-β-CD. Thus, for the acetylated β-CDs the hydrophobic cavities showed an opposite polarization of the electron charge distribution compared to the other two CDs, phenomenon confirmed by the

opposite direction of the dipole moment vectors (β-CD & HDM-β-CD vs HDA-β-CD & HMA-β-CD) (Figure 5).

3) In the acetylated CDs, the most important HB acceptors are located at the periphery of the wider rim (C=$O_{(2)}$, C=$O_{(3)}$), whereas for β-CD and HDM-β-CD all HB acceptors belong to the backbone of the macrocycle.

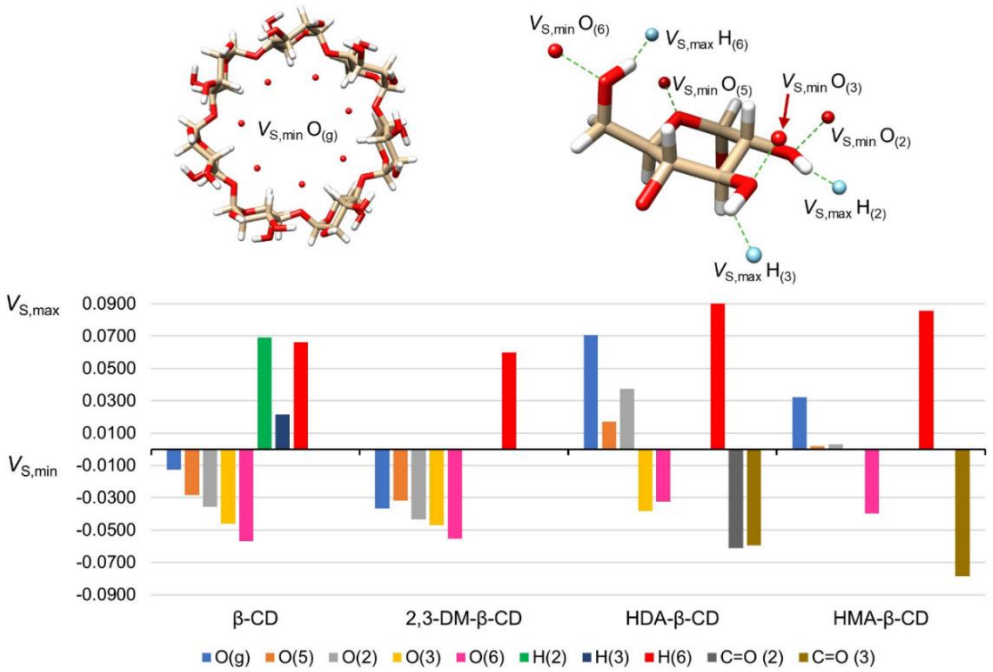

Figure 6. Location of $V_{S,min}$ and $V_{S,max}$ values calculated on the pivotal regions of each glucopyranose unit of the CDs (colour legend of the tube β-CD structure: carbon, tan; hydrogen, white; oxygen, red) and average $V_{S,max}$ and $V_{S,min}$ values [au] calculated at DFT level [B3LYP/6-31G(d)] for the $O_{(g)}$, $O_{(5)}$, $O_{(2)}$, $O_{(3)}$, $O_{(6)}$, O$\underline{H}_{(2)}$, O$\underline{H}_{(3)}$, O$\underline{H}_{(6)}$, C=$\underline{O}_{(2)}$, and C=$\underline{O}_{(3)}$ atoms of β-CD, HDM-β-CD, HDA-β-CD, and HMA-β-CD (for numerical values see Tables S5, S9, S17, and S25, supporting information).

Based on the results of the computational analysis, it appeared that for the enantioseparation of the tetramisole enantiomers by derivatized β-CDs, and likely for other structurally similar analytes (Chankvetadze et al., 2003), the selectivity increased with the macrocycle flexibility favoring the penetration of the analyte into the cavity and a conformational adjustment stabilizing the CD-analyte complexes. In terms of stereoelectronic properties, acetylation at the wider rim induced a redistribution of the electron charge density in the resulting CDs. As observed in CE outcomes, this impacted on both binding and enantioselectivity.

4.3.2 Quantum mechanics optimized structures of the complexes of tetramisole enantiomers with native and derivatized β-CDs

A critical point in the modeling of selectand-CD complexes is the preparation of the proper structures of such complexes as input files for the subsequent QM optimization. This preliminary step should require an acceptable computational cost, and the choices made in this regard should allow for obtaining low-energy conformers as close as possible to the global DFT minimum (Mazurek & Szeleszczuk, 2022). When crystal structures of the complexes are not available as it is very common, in most cases the

initial structure is identified by molecular docking performed in the MM domain, or by manual docking of the analyte into the macrocycle cavity. Molecular docking of a single structure is in general not sufficient to obtain a reliable input file for QM calculations, and the QM minimization of different conformers is generally required. Although the application of this approach substantially increases computational time, it represents an interesting way to inspect the energy of a complex structure at different penetration degrees of the analyte within the cavity of a macrocyle.

In general, for a chiral analyte featuring an unsubstituted phenyl ring, the aromatic moiety enters the CD cavity through the wider rim (Armstrong & DeMond, 1984; Chankvetadze 2003; Lomsadze et al., 2012). On the other hand, experimental and computational studies showed that for chiral analytes having substituted phenyl rings, the aromatic moiety does not fit into the HDA-β-CD through the wider rim remaining exposed to the bulk solvent. This was observed, for example, for clenbuterol (Chankvetadze et al., 2003) and clenpenterol (Salgado et al., 2017).

We started our investigation by studying the complexes of the tetramisole enantiomers with β-CD as a model for developing the computational protocol for the 2,3-disubstituted CDs. Given the presence of an unsubstituted phenyl ring in tetramisole, our starting hypothesis was that the selectand enantiomers enter the CD cavity by directing the phenyl ring toward the wider rim of the macrocyle. On this basis, four structures for each (*R*)- and (*S*)-tetramisole/β-CD complex were built, which featured different penetration degrees of the enantiomers in the CD cavity. These eight structures were used as input files for subsequent DFT geometry optimization at DFT level of theory by using B3LYP/6-31G(d,p) as model chemistry and SMD (water) as solvation model. In Figure 7, the four input files built for the (*R*)-tetramisole/β-CD complex are depicted.

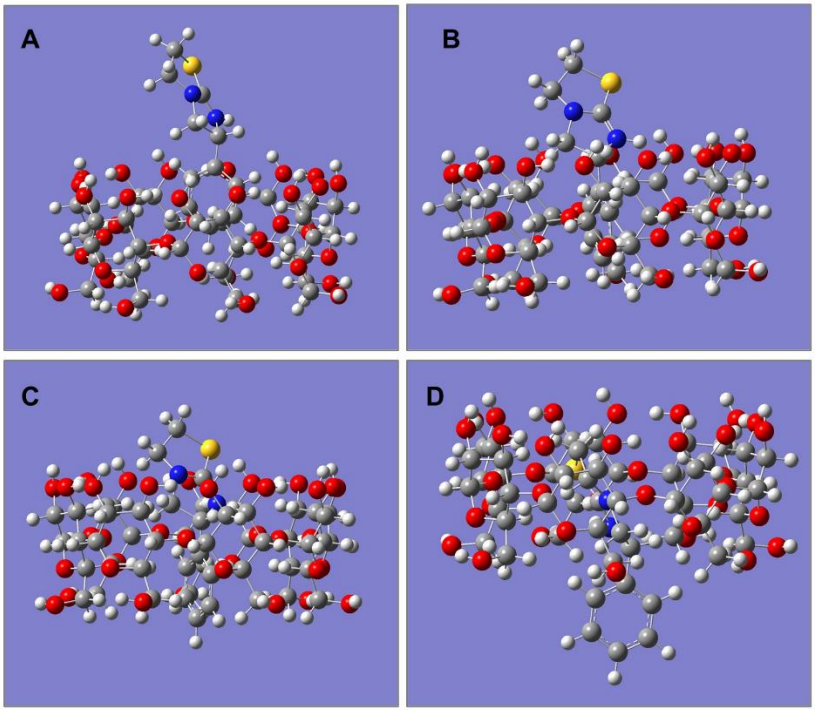

Figure 7. Structures of the (*R*)-tetramisole/β-CD complex, manually docked with different penetration degrees in the CD cavity as input files for the DFT geometry optimization of the complex (colour legend: carbon, grey; hydrogen, pale grey; nitrogen, blue; oxygen, red; sulphur, yellow).

Overall, the applied protocol consists of four steps: *a*) a preliminary search of the lowest-energy structure of the complex using four structures featuring different penetration degree of the analyte in the CD cavity as input files (including SMD solvation); *b*) frequency calculation of the lowest-energy structure determined for each complex to confirm the absence of imaginary frequency and, consequently, the achievement of real minima at the stationary point; *c*) optimization of the structures computed with the SMD solvation by including the *gd3* correction for dispersion; *d*) determination of the $E_{binding}$ and $\Delta E_{binding}$ values related to the lowest-energy structures computed for each diastereomeric complex with and without dispersion correction. The application of this protocol allowed us to determine the energetic profile associated with the dynamic penetration of the analyte into the CD cavity (Figure 8A) and to gain information about the structural effects determining increments or lowering of the total electronic energy during the optimization steps (Figure 8B).

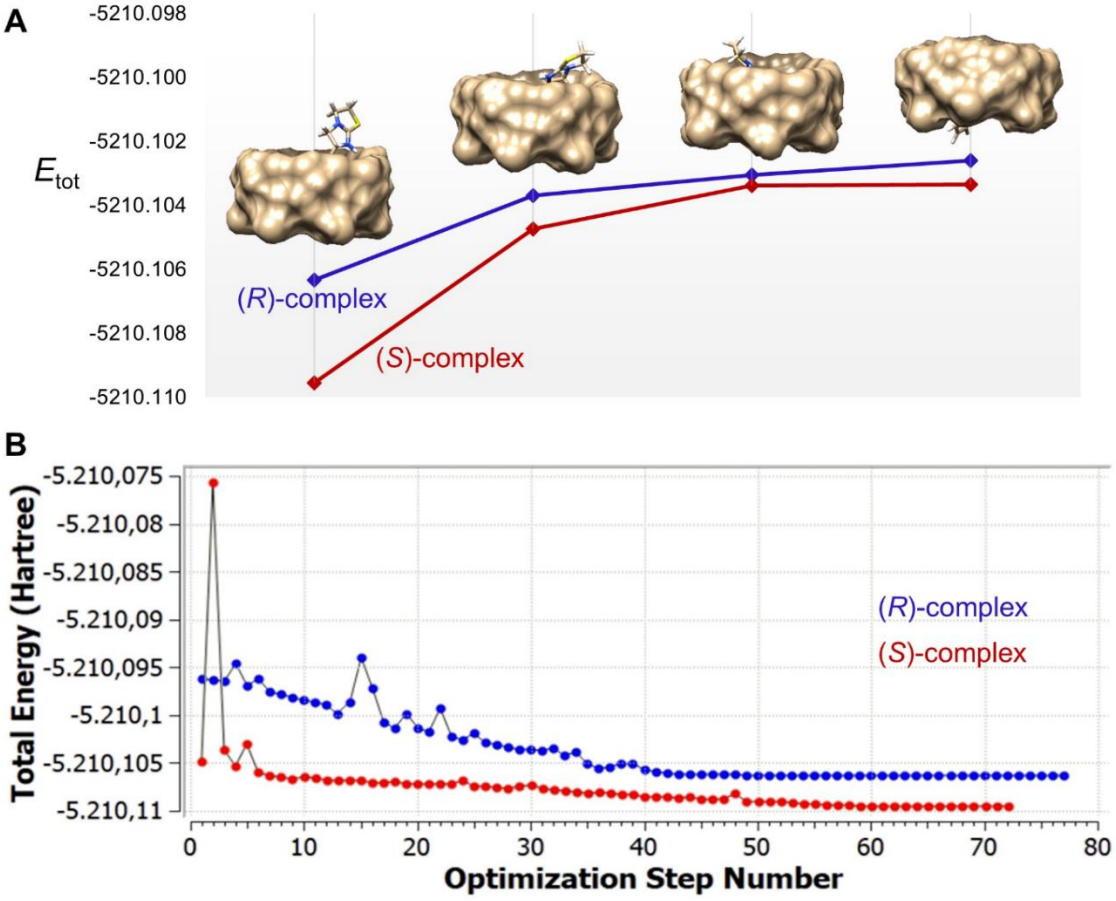

Figure 8. (A) Energy profile associated with the dynamic penetration of the tetramisole enantiomers into the cavity of β-CD, and (B) dependence of the total electronic energy on the optimization steps (and related structural changes).

The complexes of tetramisole with the 2,3-disubstituted β-CDs were treated according to the same protocol. The results in terms of lowest-energy structures computed for the eight diastereomeric complexes, $E_{binding}$ and $\Delta E_{binding}$ and calculated EMOs of the computed complexes, and related noncovalent interactions are reported in Figure 9, Table 4, and Table 5, respectively. The total electronic energies computed for each complex are reported in Table S28 (supporting information).

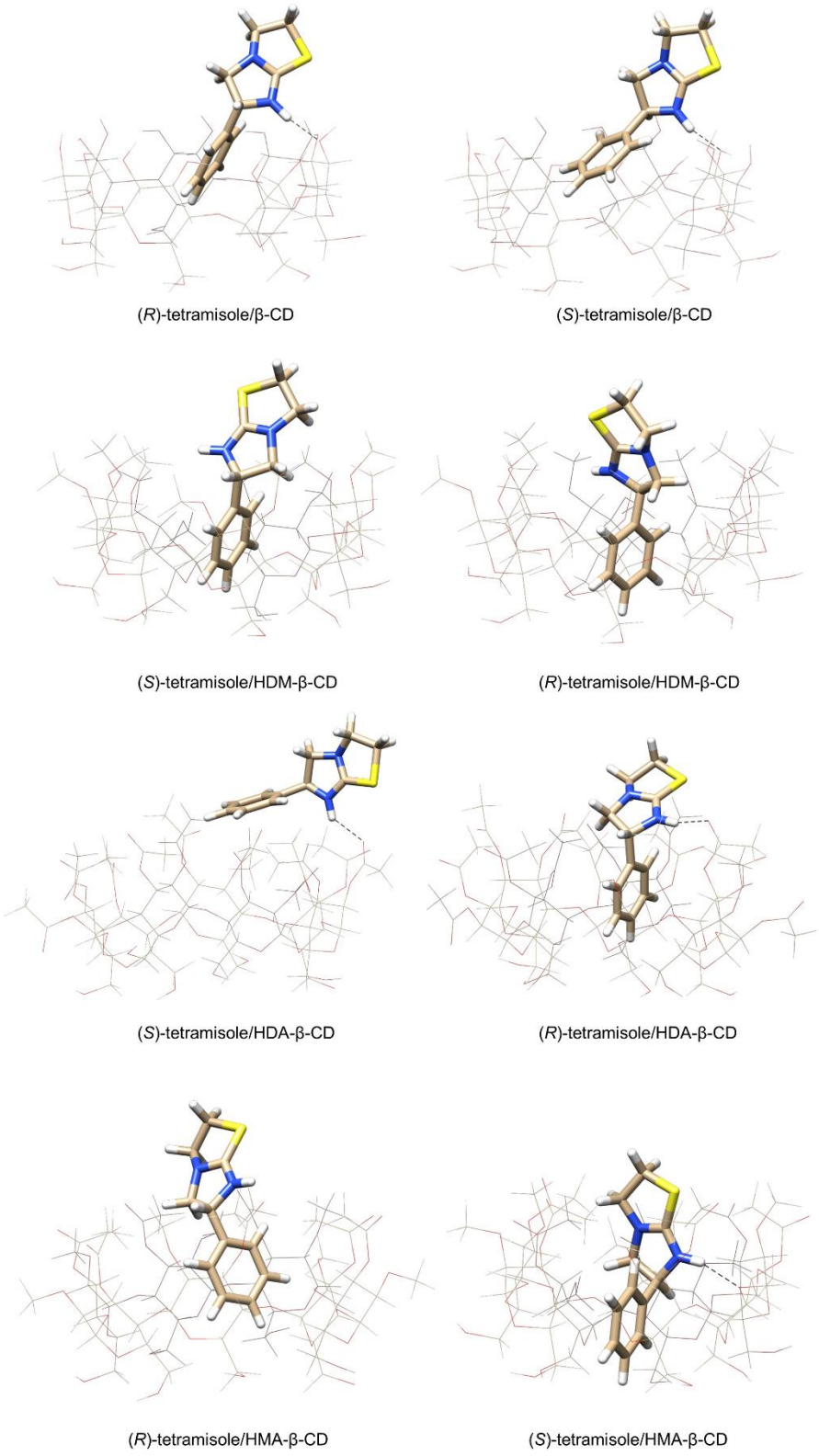

548

549 **Figure 9.** Optimized structures of the complexes of tetramisole with β-CD, HDM-β-CD, HDA-β-CD, and
550 HMA-β-CD [DFT/B3LYP/6-31G(d,p), SMD, water]. β-CD and HDM-β-CD complexes without *gd3*
551 correction; HDA-β-CD, and HMA-β-CD with *gd3* correction.

The data were examined considering their agreement with the experimental data by comparing three pairs of experimental and computed descriptors: *a)* experimental $EMO_{exp.}$ and calculated $EMO_{calc.}$, *b*) migration time of the enantiomers and $E_{binding}$ of the corresponding complex, and *c*) selectivity and $\Delta E_{binding}$ for each pair of diastereomeric complexes. On this basis, among the computed data obtained with and without the dispersion correction, two different boundary conditions applied to the adopted model chemistry were found to provide the best results in terms of consistency with the experimental data: *a*) DFT/B3LYP/6-31G(d,p)/SMD (water) for β-CD and HDM-β-CD, and *b*) DFT/B3LYP/6-31G(d,p)/SMD (water)/*gd3* for HDA-β-CD and HMA-β-CD. In general, the effect of introducing dispersion correction was a deeper penetration of the selectand into the CD cavity and an increase of the $E_{binding}$ values.

Table 4. DFT binding energies ($E_{binding}$), binding energy differences ($\Delta E_{binding}$), and EMO computed for the inclusion complexes of (*R*)- and (*S*)-tetramisole with β-CD, HDM-β-CD, HDA-β-CD, and HMA-β-CDs in the gas phase, with the SMD solvation, and with the *gd3* dispersion correction. The experimental EMO is reported for comparison.

		$E_{binding}$ (kcal·mol^{-1})	Tetramisole/CD			
CD	QM	(*R*)-complex	(*S*)-complex	$\Delta E_{binding}$ (kcal·mol^{-1})	$EMO_{calc.}$	$EMO_{exp.}$
β-CD	SMD	-6.69	-8.70	-2.01	(*R*)>(*S*)	(*R*)>(*S*)
HDM-β-CD	SMD	-15.57	-15.53	-0.04	(*S*)>(*R*)	ns[a]
HDA-β-CD	SMD/*gd3*	-40.88	-29.69	-11.19	(*S*)>(*R*)	(*S*)>(*R*)
HMA-β-CD	SMD/*gd3*	-36.77	-51.10	-14.33	(*R*)>(*S*)	(*R*)>(*S*)

[a]not separated

On this basis, the following conclusions were drawn:

1) The computed data showed that the development of a reasonably reliable QM model able to describe different complexes, featuring distinctive structural features and interaction capability, may require the application of different computational boundary conditions. Thus, the introduction of the dispersion correction in the adopted model chemistry appeared useful for describing the behaviour of the acetylated CDs. The necessity to use different computational methods to properly describe very similar molecular systems was also reported for other host-guest complexes (Assaf et al., 2017).
2) In all cases, the $EMO_{calc.}$ were fully consistent with $EMO_{exp.}$. This was also true for HDM-β-CD. In this case, a $\Delta E_{binding}$ = -0.04 kcal·mol^{-1} was obtained for the diasteromeric complexes, which agrees with the absence of enantioseparation at a low concentration of the CD (17.6 mM). However, the (*S*)>(*R*) migration order obtained as $EMO_{calc.}$ was consistent with the $EMO_{exp.}$ observed in CE by using the chiral selector at a high concentration (112.7 mM) (Figure S1, supporting information).
3) The $E_{binding}$ values decreased following the order (*R*)-tetramisole/β-CD > (*S*)-tetramisole/β-CD > (*S*)-tetramisole/HDA-β-CD > (*R*)-tetramisole/HDA-β-CD > (*S*)-tetramisole/HMA-β-CD, with a trend consistent with the experimental migration times of tetramisole observed in CE [t_m (min), $E_{binding}$ (kcal·mol^{-1}): (*R*)/β-CD, 4.094, -6.69; (*S*)/β-CD, 4.171, -8.70; (*S*)/HDA-β-CD, 4.481, -29.69; (*R*)/HDA-β-CD, -5.230, 40.88; (*S*)/HMA-β-CD, 5.927, -51.10]. Otherwise, some

discrepancies could be observed in the values of binding energies related to the (*R*)- and (*S*)-tetramisole/HDM-β-CD, and the (*R*)-tetramisole/HMA-β-CD complexes with respect to the other CD-complexes. Concerning the HDM-β-CD complexes, the calculations appeared to overestimate the $E_{binding}$ values, which were not consistent with the short migration time of tetramisole observed in CE with this CD (t_m = 3.748 min). On the other hand, longer migration times were observed in CE when using a high concentration of HDM-β-CD (t_m (S) = 6.31 min; t_m (*R*) = 6.44 min).

Table 5. Noncovalent interactions and related lengths (Å) observed in the inclusion complexes of (*R*)- and (*S*)-tetramisole with β-CD, HDM-β-CD, HDA-β-CD, and HMA-β-CDs computed at DFT level of theory.

		NCI[a]	Distance (Å)		
CD	QM	CD···enantiomer	(*R*)-complex	(*S*)-complex	EMO_{exp}
β-CD	SMD	**O(2)···H-N**	**1.861**		(*R*)>(*S*)
		O(3)···H-N		**1.754**	
		H(3)···H_{Ar}(*o*)	2.396	2.363	
		H(3)···H_{Ar}(*m*)		2.266, 2.300	
		H(5)···H_{Ar}(*m*)	2.704		
		H(5)···H_{Ar}(*m*)	2.594		
		H(5)···H_{Ar}(*p*)		2.912	
HDM-β-CD	SMD	OMe(3)···H-CHN	2.334	2.968	ns[b]
		OMe(2)···H-CHN		2.489	
		OMe(3)···H-N		2.394	
		H(3)-H···H-N	2.702		
		H(3)···H-CHN	2.560	2.457	
		H(3)···H-C*	2.781		
		H(3)···H_{Ar}(*o*)		2.366	
		H(5)···H_{Ar}(*m*)	2.338, 2.330	2.276, 2.415	
		H(5)···H_{Ar}(*o*)		2.674	
HDA-β-CD	SMD/*gd3*	**C=O(2)···H-N**	**1.854**	**2.011**	(*S*)>(*R*)
		OMe(2)···H-CHS	2.214		
		OMe(3)···H-CHN	2.193, 2.918		
		OMe(3)···H-C*	2.393		
		OMe(2)···H_{Ar}(*m*)		2.105	
		OMe(3)···H_{Ar}(*p*)		2.435	
		OMe(3)···H_{Ar}(*o*)	2.278	2.619	
		OMe(2)···H_{Ar}(*o*)	2.303		
		O(g)···H_{Ar}(*m*)	**2.353**		
		H(5)···H_{Ar}(*p*)	2.574		
		$HOCH_2$···H_{Ar}(*m*)	2.129		
HMA-β-CD	SMD/*gd3*	**O(g)···H-N**		**1.943**	(*R*)>(*S*)
		OMe(3)···H-CHS		2.676	
		OMe(3)···H-CHN	2.387, 2.535	2.233	
		OMe(2)···H-CHN		2.630	
		O(g)···H-CHN		**2.530**	
		OMe(3)···H-N	2.411		
		OMe(3)···H-C*	2.407		
		H(5)···H-C*		2.391	
		OMe(3)···H_{Ar}(*o*)	2.440	2.318	
		H(5)···H_{Ar}(*m*)		2.094	
		H(5)···H_{Ar}(*p*)	2.381	2.550	
		H(3)···H_{Ar}(*m*)	2.246		
		H(3)···H_{Ar}(*o*)	2.924		
		H(5)···H_{Ar}(*o*)		2.701	
		$HOCH_2$···H_{Ar}(*m*)	2.306		

[a]Noncovalent interactions, NCI
[b]not separated

4) The $\Delta E_{binding}$ values decreased following the order tetramisole/HDM-β-CD > tetramisole/β-CD > tetramisole/HDA-β-CD > tetramisole/HMA-β-CD. Thus, except for HMA-β-CD, the overall trend is consistent with the experimental selectivity α observed in CE in both cases [α, $\Delta E_{binding}$ (kcal·mol^{-1}): HDM-β-CD, 1.00, -0.04; β-CD, 1.02, -2.01; HDA-β-CD, 1.17, -11.19; HMA-β-CD, 1.05, -14.33]. The obvious discrepancy observed for the HMA-β-CD and HDA-β-CD complexes indicates that the values determined for HMA-β-CD are rather overestimated. This incongruence may be explained by the fact that the complexes of methylated HDM-β-CD and acetylated HDA-β-CD were described by two different boundary conditions applied in the model chemistry, using the dispersion correction only for the acetylated CD. Thus, each boundary condition may be insufficient to fully describe correctly the energy related to the HMA-β-CD complexes, which contain both methyl and acetyl groups at the wider rim.
5) Although limitations of QM methods to compute the total energy in a solvated environment exist, this technique is essential to study noncovalent interactions dependent on the electronic structures of the interacting partners. HBs and weak HBs along with H···H dispersion-based noncovalent interactions were observed in the lowest-energy computed complexes (Table 5). The noncovalent interaction patterns (Figure 9) showed a pivotal role of HBs as enantioselective noncovalent interactions contributing to a differentiation between the two transient diastereomeric complexes. Indeed, whereas HBs could be observed in the (*R*)-tetramisole/β-CD, (*S*)-tetramisole/β-CD, (*R*)-tetramisole/HDA-β-CD, (*S*)-tetramisole/HDA-β-CD, and (*S*)-tetramisole/HMA-β-CD complexes with a strength consistent with the experimental CE results, no HB was observed in the complexes of (*R*)-and (*S*)-tetramisole with the HDM-β-CD, which did not enantioseparate tetramisole in CE at a low concentration. On one hand, the pattern confirmed the importance of HB interactions for the binding of the guest to the chiral selector and for its enantiodifferentiation in the aqueous environment. On the other hand, the noncovalent interaction patterns featured multiple weak interactions likely acting cooperatively in both binding and enantiorecognition processes.
6) In the case of the tetramisole/β-CD complexes, the relative strength of the HBs in each complex, lower for the (*R*)-complex ($d_{O(2)\cdots H\text{-}N}$ = 1.861 Å) compared to the (*S*)-complex ($d_{O(3)\cdots H\text{-}N}$ = 1.754 Å), was consistent with the higher nucleophilic properties computed for (O)(3) compared to the O(2) atoms as acceptors ($V_{S,min}$ O(3) = -0.0460 Hartree) > $V_{S,min}$ O(2) = -0.0357 Hartree).
7) Focusing on the tetramisole/HDA-β-CD complexes (Figure 9), it was interesting to note that the inclusion of the (*S*)-enantiomer appeared to be energetically disfavoured, whereas the contribution of dispersion forces could enhance the inclusion process for the (*R*)-enantiomer. Despite this substantial difference, a N-H···O=C(2) HB between analyte and selector was observed in both structures. The presence of a HB between the N-H of the analyte and the carbonyl oxygen at the 2-position suggested that this interaction may control the inclusion of the analyte at the wider rim, evidencing a pivotal function of the acetyl groups decorating the CD. However, an opposite effect of this interaction may be envisaged. On one side, the N-H···O=C(2) HB "captures" the analyte and moves it to the proximity of the rim. On the other

hand, it may prevent a deeper inclusion of the analyte into the cavity. In this context, the effect of dispersion forces appeared to be pivotal to favour the inclusion process. It is worth mentioning that, starting from the same input file, in the gas phase or by introducing the solvation model (without *gd3* correction), the optimization process pulled the analyte out of the CD cavity (data not shown). Similar observations were made earlier when modeling the inclusion complex of clenpenterol with HDA-β-CD (Salgado et al., 2017).

8) The key role of the C=O(2) oxygen atoms, as HB acceptors, observed for HDA-β-CD may explain the higher enantiodifferentiation ability of the HDA-β-CD compared to HMA-β-CD which has a methyl group in place of the acetyl group at the 2-OH position of the wider rim. This structural effect likely affected the enantiodifferentiation ability of HMA-β-CD. HBs involving the O(g) oxygen atoms of the macrocycle were observed in the (*S*)-tetramisole/HMA-β-CD complex. These HBs contributed to keeping the enantiomer inside the cavity increasing its affinity toward the CD. However, the HBs were not so effective for the enantiorecognition compared to the HBs involving the acetyl groups at the wider rim as observed for the HDA-β-CD complexes. This indicated that for HMA-β-CD the synergistic function of methyl and acetyl groups in determining the higher affinity of tetramisole toward this CD may be considered apparent. However, the co-presence of acetyl and methyl groups at the wider rim induced structural modifications, which resulted in a change of both binding and recognition mechanisms of the CD compared to HDA-β-CD.

In light of the results emerging from the computational analysis, it is interesting to summarize the results obtained in CE and NMR analyses. In CE, drastic differences in the selectivity of binding of tetramisole enantiomers were observed between β-CD and HDA-β-CD on both qualitative and quantitative levels. First, the enantiomer affinity patterns of tetramisole towards these two CDs were opposite to each other. In addition, when used in equimolar amounts, β-CD provided a separation factor of just 1.02, while in the case of HDA-β-CD this was 1.17 (Figure 1C). These drastic differences observed in CE were consistent with the results obtained based on ^{1}H NMR spectroscopy (Figure 2). On the other hand, the structures computed for both β-CD and HDA-β-CD agreed perfectly with the results of NMR spectroscopy and with the CE outcomes. Indeed, whereas the computed complexes of tetramisole enantiomers with β-CD showed rather similar structure, in the case of HDA-β-CD the computed complexes featured very different structures (Figure 9). Since such significant differences between the structures of the two enantiomers with the same CD are very rarely observed, we attempted to confirm this phenomenon by ROESY experiments. The ROESY results shown in Figure 10 confirmed some NOE effects between the aromatic proton at the *orto*-position of (*S*)-tetramisole and the H-3 protons of HDA-β-CD (Figure 10D). Coherently, distances consistent with NOE interactions were measured between these hydrogen atoms within the computed (*S*)-tetramisole/HDA-β-CD complex (4.86 and 5.33 Å). Thus, based on this computed structure, a weak NOE effect between the (*S*)-tetramisole aromatic proton and the HDA-β-CD H-3 proton appeared to be possible. Consequently, the structures computed for the tetramisole/HDA-β-CD complexes (Figure 9) appeared to be well supported by the NMR spectroscopy data.

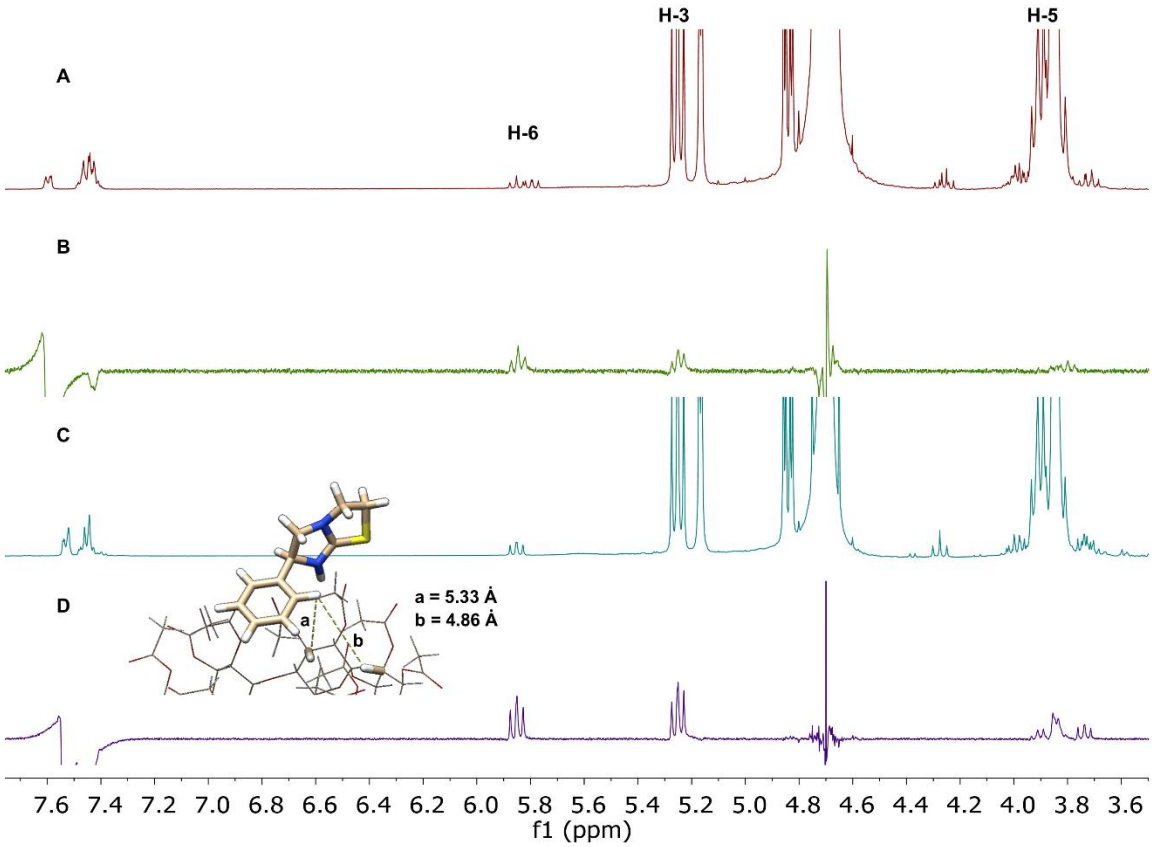

Figure 10. Expanded partial ^{1}H NMR (A,C) and ROESY (B,D) spectra showing the signals of tetramisole H-6 and HDA-β-CD H-3 and H-5 within the complexes of HDA-β-CD with racemic tetramisole (A,B) and (*S*)-tetramisole (C,D). A structure describing the short contacts measured in the computed (*S*)-tetramisole/HDA-β-CD complex is also inserted. Experimental conditions: 400 MHz, 25°C; sample A: 1.0 mg (*R*,*S*)-tetramisole and 16.0 mg HDA-β-CD in 1.0 mL 100 mM D_3PO_4 buffer (pH 3.0, TEA); sample B: 2 mg (*S*)-tetramisole and 32.0 mg HDA-β-CD in 1.0 mL 100 mM D_3PO_4 buffer (pH 3.0, TEA).

5 Conclusions

In agreement with the initial hypotheses, by using NMR spectroscopy and QM calculations, some factors contributing to the binding and enantiorecognition mechanisms underlying the enantioseparations observed in CE could be identified and quantified. NMR spectroscopy and QM calculations provided strong evidence supporting the superior enantioselective recognition ability observed in CE for the HDA-β-CD compared to β-CD. As indirectly shown on Figure 2, β-CD forms complexes with rather similar structure with (*S*)- and (*R*)-tetramisole (Figure 9), while the structures of the complexes in the case of HDA-β-CD are very different (Figure 9).

Although further investigations are needed to obtain calculated free energy differences of the same order compared to the small experimental values, the computational results obtained in this study showed definitely that derivatization of the wider rim of the β-CD impacts the inter- and intramolecular interactions of the entire macrocycle, not only the derivatized secondary rim.

For acetylated CDs, a distinctive balance between HBs and multiple H···H interactions based on dispersion underlay the enantioseparation processes, while in the case of nonacetylated CDs this was not the case. On this basis, although the use of the same model chemistry is recommended when different molecular systems are compared, the addition of dispersion corrections to the selected model chemistry was shown to improve the model for the acetylated CDs.

In the case of β-CD, the contribution of HBs appeared dominant compared to dispersion-based interactions. Consequently, the introduction of the *gd3* correction overestimated the dispersion contribution, which apparently does not significantly contribute in the "real" system. On the other hand, for the β-CD complexes computed with the *gd3* correction, a less negative $\Delta E_{binding}$ value (-1.62 kcal·mol^{-1}) was found compared to that computed without the dispersion correction (-2.01 kcal·mol^{-1}). This indicated that dispersion forces, if present, would oppose the HB function in the enantioseparation process. For HDA-β-CD, the opposite was true. In this case, the contribution of dispersion forces appeared to be dominant compared to HBs, so that the introduction of the *gd3* correction properly accounted for this contribution. On the other hand, for the HDA-β-CD complexes computed without the *gd3* correction, a negative $\Delta E_{binding}$ value much less (-0.29 kcal·mol^{-1}) compared to the value computed without the dispersion correction (-11.18 kcal·mol^{-1}) was obtained. Importantly, HBs would oppose dispersion forces in the enantioseparation process in case of a major effect. Thus, at the molecular level, computing the complexes without the *gd3* correction resulted in a reversed EMO [(*R*)>(*S*)] compared to the experimental EMO [(*S*)>(*R*)] because within the CD complex of the first migrating (*S*)-enantiomer (d_{HB} = 1.909 Å), a stronger HB compared to the HB within the complex of the second migrating (*R*)-enantiomer (d_{HB} = 1.935 Å) was observed. Both HBs kept the enantiomers in the proximity of the wider rim, preventing its inclusion in the cavity.

CRediT authorship contribution statement

Ani Rurua: Investigation, Data curation. **Mariam Shanidze**: Investigation, Data curation. **Nutsa Tsetskhladze**: Formal analysis, Data curation. **Antonio Salgado**: Methodology, Investigation, Data curation. **Paola Peluso**: Conceptualization, Methodology, Formal analysis, Writing – Review & Editing. **Roberto Dallocchio**: Formal analysis, Data curation. **Gerhard K.E. Scriba**: Data curation, Writing – Review & Editing. **Milo Malanga**: Resources. **Szabolcs Beni**: Resources. **Bezhan Chankvetadze**: Conceptualization, Methodology, Project administration, Supervision, Funding acquisition, Writing – original draft, Writing – Review & Editing.

Acknowledgements

Bezhan Chankvetadze thanks Shota Rustaveli National Science Foundation of Georgia for a partial support of this study through the grant N° FR-23-24319 for fundamental research. Szabolcs Beni has received funding from the European Union's Horizon Europe research and innovation programme under the Marie Sklodowska-Curie grant agreement Bicyclos N° 101130235.

Conflict of interest

The authors declare that they have no known competing financial interests or personal relationships that could have appeared to influence the work reported in this paper.

Data availability statement

The data that support the findings of this study are available from the corresponding author upon reasonable request.

5 References

Alexander, J. M., Clark, J. L., Brett, T. J., & Stezowski, J. J. (2002) Chiral discrimination in cyclodextrin complexes of amino acid derivatives: β-cyclodextrin/*N*-acetyl-L-phenylalanine and *N*-acetyl-D-phenylalanine complexes. *The Proceedings of the National Academy of Sciences*, *99*, 5115-5120. https://doi.org/10.1073/pnas.07264759

Armstrong, D. W., & DeMond, W. (1984). Cyclodextrin bonded phases for the liquid chromatographic separation of optical, geometrical and structural isomers. *Journal of Chromatographic Science*, *22*, 411-415. https://doi.org/10.1093/chromsci/22.9.411

Assaf, K. I., Florea, M., Antony, J., Henriksen, N. M., Yin, J., Hansen, A., Qu, Z. -W., Sure, R., Klapstein, D., Gilson, M. K., Grimme, S., & Nau, W. M. (2017). HYDROPHOBE Challenge: A joint experimental and computational study on the host−guest binding of hydrocarbons to cucurbiturils, allowing explicit evaluation of guest hydration free-energy contributions. *The Journal of Physical Chemistry B*, *121*, 11144-11162. https://doi.org/10.1021/acs.jpcb.7b09175.

Blaschke, G., & Chankvetadze, B. (2000). Resolution of racemic mixtures. In F. Gualtieri (Ed.), *New Trends in Synthetic Medicinal Chemistry* (pp. 139-273). Wiley-VCH, Weinheim, Germany.

Cai, W., Sun, T., Shao, X., & Chipot, C. (2008). Can the anomalous aqueous solubility of β-cyclodextrin be explained by its hydration free energy alone? *Physical Chemistry Chemical Physics*, *10*, 3236-3243. https://doi.org/10.1039/b717509d

Casas-Hinestroza, J. L., Bueno, M., Ibáñez, E., & Cifuentes, A. (2019). Recent advances in mass spectrometry studies of non-covalent complexes of macrocycles - A review. *Analytica Chimica Acta*, *1081*, 32-50. https://doi.org/10.1016/j.aca.2019.06.029

763 Chankvetadze, B. (1997). Separation selectivity in chiral capillary electrophoresis with charged
764 selectors. *Journal of Chromatography A*, *792*, 269-295. https://doi.org/10.1016/S0021-
765 9673(97)00752-8

766 Chankvetadze, B. (1999). Recent trends in chiral separations using capillary electromigration
767 techniques. *Trends in Analytical Chemistry*, *18*, 485-498. https://doi.org/10.1016/S0165-
768 9936(99)00121-1

769 Chankvetadze, B. (2004). Combined approach using capillary electrophoresis and NMR spectroscopy
770 for an understanding of enantioselective recognition mechanisms by cyclodextrins. *Chemical*
771 *Society Reviews*, *33*, 337-347. https://doi.org/10.1039/B111412N

772 Chankvetadze, B. (2018). Contemporary theory of enantioseparations in capillary electrophoresis.
773 *Journal of Chromatography A*, *1567*, 2-25. https://doi.org/10.1016/j.chroma.2018.07.041

774 Chankvetadze, B., & Blaschke, G. (2001) Enantioseparations in capillary electromigration techniques:
775 Recent developments and future trends. *Journal of Chromatography A*, *906*, 309-363.
776 https://doi.org/10.1016/S0021-9673(00)01124-9

777 Chankvetadze, B., Burjanadze, N., Bergenthal, D., Breitkreutz, J., Bergander, K., Kataeva, O., Fröhlich,
778 R., & Blaschke, G. (2002a). Mechanistic study on the opposite migration order of the enantiomers
779 of ketamine with α- and β-cyclodextrin in capillary electrophoresis. *Journal of Separation Science*,
780 *25*, 1155-1166. https://doi.org/10.1002/1615-9314(20021101)25:15/17<1155::AID-
781 JSSC1155>3.0.CO;2-M

782 Chankvetadze, B., Burjanadze, N., Maynard, D.M., Bergander, K., Bergenthal, D., & Blaschke, G.
783 (2002b). Comparative enantioseparations with native β-cyclodextrin and heptakis-(2-*O*-methyl-
784 3,6-di-*O*-sulfo)-β-cyclodextrin in capillary electrophoresis. *Electrophoresis*, *23*, 3027-3034.
785 https://doi.org/10.1002/1522-2683(200209)23:17<3027:AID-ELPS3027>3.0.CO;2-V

786 Chankvetadze, B., Burjanadze, N., Pintore, G., Strickmann, D., Bergenthal, D., & Blaschke, G. (1999).
787 Chiral recognition of verapamil by cyclodextrins studied with capillary electrophoresis, NMR- and
788 mass-spectrometry. *Chirality*, *11*, 635-644. https://doi.org/10.1002/(SICI)1520-
789 636X(1999)11:8<635:AID-CHIR5>3.0.CO;2-D

790 Chankvetadze, B., Lomsadze, K., Burjanadze, N., Breitkreutz, J., Pintore, G., Chessa, M., Bergenthal,
791 D., Bergander, K., & Blaschke, G. (2003). Comparative enantioseparations with native β-
792 cyclodextrin, randomly acetylated β-cyclodextrin and heptakis-(2,3-di-O-acetyl)-β-cyclodextrin in
793 capillary electrophoresis. *Electrophoresis*, *24*, 1083−1091.
794 https://doi.org/10.1002/elps.200390126

795 Chankvetadze, B., Pintore, G., Burjanadze, N., Bergenthal, D., Bergander, K., Breitkreutz, J.,
796 Mühlenbrock, C., & Blaschke, G. (2000) Mechanistic study of opposite migration order of
797 dimethindene enantiomers in capillary electrophoresis in the presence of native β-CD and
798 heptakis-(2,3,6-tri-*O*-methyl)-β-CD. *Journal of Chromatography A*, *875*, 455-469.
799 https://doi.org/10.1016/S0021-9673(00)00146-1

800 Chankvetadze, B., & Scriba, G.K.E. (2023). Cyclodextrins as chiral selectors in capillary
801 electrophoresis: recent trends in mechanistic studies. *Trends in Analytical Chemistry*, *160*,
802 116987. https://doi.org/10.1016/j.trac.2023.116987

803 Chen, F., Gülbakan, B., Weidmann, S., Fagerer, S. R., Ibáñez, A. J., & Zenobi, R. (2016) Applying mass
804 spectrometry to study non-covalent biomolecule complexes. *Mass Spectrometry Reviews*, *35*,
805 48-70. https://doi.org/10.1002/mas.21462

806 Coleman, A. W., Nicolis, I., Keller, N., & Dalbiez, J. P. (1992) Aggregation of cyclodextrins: an
807 explanation of the abnormal solubility of β-cyclodextrin. *Journal of Inclusion Phenomena and*
808 *Macrocyclic Chemistry*, *13*, 139-143. https://doi.org/10.1007/BF01053637

809 Dallocchio, R., Dessì, A., Sechi, B., & Peluso, P. (2023). Molecular dynamics simulations of amylose-
810 and cellulose-based selectors and related enantioseparations in liquid phase chromatography.
811 *Molecules*, *28*, 7419. https://doi.org/10.3390/molecules28217419

812 Fejős, I., Kalydi, E., Malanga, M., Benkovics, G., & Béni, S. (2020). Single isomer cyclodextrins as chiral
813 selectors in capillary electrophoresis. *Journal of Chromatography A*, *1627*, 461375.
814 https://doi.org/10.1016/j.chroma.2020.461375

815 Foresman, G. B., & Frisch, Æ. (2015). *Exploring Chemistry with Electronic Structure Methods* (3rd ed.).
816 Gaussian, Inc., Wallingford, CT USA, p. 209.

817 Gaussian 16, Revision C.01, Frisch, M. J., Trucks, G. W., Schlegel, H. B., Scuseria, G. E., Robb, M. A.,
818 Cheeseman, J. R. et al. (2016). Gaussian, Inc., Wallingford CT.

819 Gogolashvili, A., Lomsadze, K., Chankvetadze, L., Takaishvili, N., Peluso, P., Dallocchio, R., Salgado,
820 A., & Chankvetadze, B. (2021). Separation of tetrahydrozoline enantiomers in capillary
821 electrophoresis with cyclodextrin-type chiral selectors and investigation of chiral recognition
822 mechanism. *Journal of Chromatography A*, *1643*, 462084.
823 https://doi.org/10.1016/j.chroma.2021.462084

824 Grimme, S., Antony, J., Ehrlich, S., & Krieg, H. (2010). A consistent and accurate ab initio
825 parametrization of density functional dispersion correction (DFT-D) for the 94 elements H-Pu.
826 *The Journal of Chemical Physics*, *132*, 154104. https://doi.org/10.1063/1.3382344

827 Grimme, S., Ehrlich, S., & Goerigk, L. (2011) Effect of the damping function in dispersion corrected
828 density functional theory. *Journal of Computational Chemistry*, *32*, 1456-1465.
829 https://doi.org/10.1002/jcc.21759

830 Hickey, A. L., Rowley, C. N. (2014) Benchmarking quantum chemical methods for the calculation of
831 molecular dipole moments and polarizabilities. *The Journal of Physical Chemistry A*, *118*,
832 678−3687. https://doi.org/10.1021/jp502475e

833 Li, W. -S., Wang, S. -C., Hwang, T. -S., & Chao, I. (2012) Substituent effect on the structural behavior
834 of modified cyclodextrin: A molecular dynamic study on methylated β-CDs. *The Journal of*
835 *Physical Chemistry B*, *116*, 3477-3489. https://doi.org/10.1021/jp207985q

836 Lomsadze, K., Domínguez Vega, E., Salgado, A., Crego, A. L., Scriba, G. K. E., Marina, M. L., &
837 Chankvetadze, B. (2012). *Electrophoresis*, *33*, 1637-1647.
838 https://doi.org/10.1002/elps.201200062

839 London, F. (1937). The general theory of molecular forces. *Transactions of the Faraday Society*, *33*, 8b-
840 26. https://doi.org/10.1039/TF937330008B

841 Mazurek, A. H., & Szeleszczuk, L. (2022). Current status of quantum chemical studies of cyclodextrin
842 host–guest complexes. *Molecules*, *27*, 3874. https://doi.org/10.3390/molecules27123874

843 Marenich, A. V., Cramer, C. J., & Truhlar, D. G. (2009) Universal solvation model based on solute
844 electron density and a continuum model of the solvent defined by the bulk dielectric constant and
845 atomic surface tensions. *The Journal of Physical Chemistry B*, *113*, 6378-6396.
846 https://doi.org/10.1021/jp810292n

847 Peluso, P., & Chankvetadze, B. (2021). Native and substituted cyclodextrins as chiral selectors for
848 capillary electrophoresis enantioseparations: Structure, features, application, and molecular
849 modeling. *Electrophoresis*, *42*, 1676–1708. https://doi.org/10.1002/elps.202100053

850 Peluso, P., & Chankvetadze, B. (2022). Recognition in the domain of molecular chirality: from
851 noncovalent interactions to separation of enantiomers. *Chemical Reviews*, *122*, 13235–13400.
852 https://doi.org/10.1021/acs.chemrev.1c00846

853 Peluso, P., Dallocchio, R., Dessì, A., Antonio Salgado, A., Chankvetadze, B., & Gerhard K.E. Scriba,
854 G.K.E. (2024). Molecular modeling study to unravel complexation of daclatasvir and its
855 enantiomer by β-cyclodextrins. Computational analysis using quantum mechanics and molecular
856 dynamics. *Carbohydrate Polymers*, *346*, 122483. https://doi.org/10.1016/j.carbpol.2024.122483

857 Peluso, P., Dessi, A., Dallocchio, R., Mamane, V., & Cossu, S. (2019). Recent studies of docking and
858 molecular dynamics simulation for liquid-phase enantioseparations. *Electrophoresis*, *40*, 1881–
859 1896. https://doi.org/10.1002/elps.201800493

860 Peluso, P., Landy, D., Nakhle, L., Dallocchio, R., Dessì, A., Krait, S., Salgado, A., Chankvetadze, B., &
861 Scriba, G. K. E. (2023). Isothermal titration calorimetry and molecular modeling study of the
862 complex formation of daclatasvir by γ-cyclodextrin and trimethyl-β-cyclodextrin. *Carbohydrate*
863 *Polymers*, *313*, 120870. https://doi.org/10.1016/j.carbpol.2023.120870

864 Perez-Miron, J., Jaime, C., & Ivanov, P. M. (2008). Molecular dynamics study on the conformational
865 flexibility and energetics in aqueous solution of methylated β-cyclodextrins. *Chirality*, *20*, 1127-
866 1133. https://doi.org/10.1002/chir.20571

867 Salgado, A., & Chankvetadze, B. (2016). Applications of nuclear magnetic resonance spectroscopy for
868 the understanding of enantiomer separation mechanisms in capillary electrophoresis. *Journal of*
869 *Chromatography A*, *1467*, 95-144. https://doi.org/10.1016/j.chroma.2016.08.060

870 Salgado, A., Tatunashvili, E., Gogolashvili, A., Chankvetadze, B., & Gago, F. (2017). Structural rationale
871 for the chiral separation and migration order reversal of clenpenterol enantiomers in capillary
872 electrophoresis using two different β-cyclodextrins. *Physical Chemistry Chemical Physics*, *19*,
873 27935-27939, https://doi.org/10.1039/c7cp04761d

Saokham, P., Muankaew, C., Jansook, P., & Loftsson, T. (2018). Solubility of cyclodextrins and drug/cyclodextrin complexes. *Molecules*, *23*, 1161. https://doi.org/10.3390/molecules23051161

Sardella, R., Camaioni, E., Macchiarulo, A., Gioiello, A., Marinozzi, M., & Carotti, A. (2020). Computational studies in enantioselective liquid chromatography: forty years of evolution in docking- and molecular dynamics-based simulations. *Trends in Analytical Chemistry*, *122*, 115703. https://doi.org/10.1016/j.trac.2019.115703

Schneider, H.J. (2019). Quantification of noncovalent interactions-promises and problems. *New Journal of Chemistry*, *43*, 15498–15512. https://doi.org/10.1039/c9nj03325d

Schneider H.J. (2022). Noncovalent interactions: A brief account of a long history. *Journal of Physical Organic Chemistry*, *35*, e4340. https://doi.org/10.1002/poc.4340

Silva, D. A., Xavier, M. J., Dutra, J. D. L., Gimenez, I. F., Freire, R. O., & da Costa Jr., N. B. (2020). Prediction of correct intermolecular interactions in host-guest systems involving cyclodextrins. *Journal of Molecular Structure*, *1205*, 127517. https://doi.org/10.1016/j.molstruc.2019.127517

Thomas, I. R., Bruno, I. J., Cole, J. C., Macrae, C. F., Pidcok, E., & Wood, P. A. (2010). WebCSD: The online portal to the Cambridge structural database. *Journal of Applied Crystallography*, *43*, 362-366. https://doi.org/10.1107/S0021889810000452

Varfaj, I., Labikova, M., Sardella, R., Hettegger, H., Lindner, W., Kohout, M., & Carotti, A. (2024). A journey in unraveling the enantiorecognition mechanism of 3,5-dinitrobenzoyl-amino acids with two *Cinchona* alkaloid-based chiral stationary phases: The power of molecular dynamic simulations. *Analytica Chimica Acta*, *1314*, 342791. https://doi.org/10.1016/j.aca.2024.342791

Vijayakumar, S., Kolandaivel, P. (2006) Study of static dipole polarizabilities, dipole moments, and chemical hardness for linear CH_3–$(C{\equiv}C)_n$–X (X=H, F, Cl, Br, and NO_2 and n = 1–4) molecules. *Journal of Molecular Structure: THEOCHEM*, *77*, 23-30. https://doi.org/10.1016/j.theochem.2006.04.030

Supporting information

Supporting information file: Additiona CE data, Modeling of native β-CD and methylated derivatives: Quantum mechanics data & coordinates.

Table 1. Average distances [Å] and angles [°, degree] including the related standard deviations of intramolecular HBs at the wider [inter-residue $O_{(3)}nH\cdots O_{(2)}n'$] and at the narrower [intra-residue $O_{(6)}nH\cdots O_{(5)}n$] rim, and distance between opposite glycosidic oxygen atoms [$O_{(g)}n\cdots O_{(g)}n'$] and between opposite $C_{(6)}$ atoms (narrower rim) [$C_{(6)}n\cdots C_{(6)}n'$] ($\Delta R_{l\text{-}s}$) [Å] ($1 \le n \le 7$), measured for DFT optimized β-CD, HDM-β-CD, HMA-β-CD, and HDA-β-CD structures [B3LYP/6-31G(d); SMD, water] using the Chimera version 1.16 program.

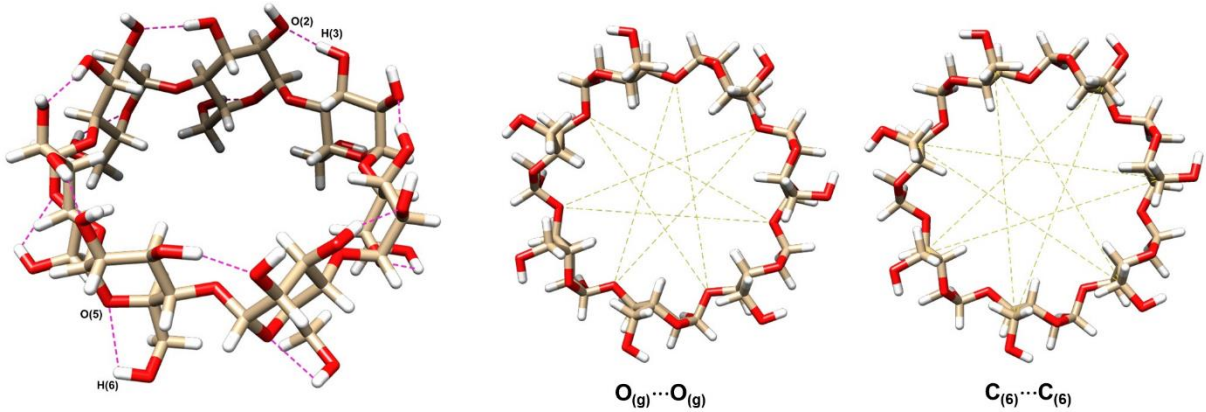

Parameter	β-CD	HDM-β-CD	HMA-β-CD	HDA-β-CD
$O_{(3)}nH\cdots O_{(2)}n'$ distance	1.864 ± 0.004			
$O_{(3)}n\text{-}H\cdots O_{(2)}n'$ angle	161.933 ± 0.444			
$O_{(6)}nH\cdots O_{(5)}n$ distance	2.424 ± 0.008	2.452 ± 0.056	2.478 ± 0.055	2.486 ± 0.044
$O_{(6)}n\text{-}H\cdots O_{(5)}n$ angle	104.747 ± 0.414	104.140 ± 1.472	103.342 ± 1.291	102.935 ± 1.208
$O_{(g)}n\cdots O_{(g)}n'$ $\Delta R_{l\text{-}s}$	0.023	1.196	1.106	1.164
$C_{(6)}n\cdots C_{(6)}n'$ $\Delta R_{l\text{-}s}$	0.312	3.940	4.053	4.559

Table 2. Average distances [Å] and angles [°, degree] including the related standard deviations of intramolecular HBs at the wider [inter-residue $O_{(3)}nH\cdots O_{(2)}n'$] and at the narrower [intra-residue $O_{(6)}nH\cdots O_{(5)}n$] rim, and distance between opposite glycosidic oxygen atoms [$O_{(g)}n\cdots O_{(g)}n'$] and between opposite $C_{(6)}$ atoms (narrower rim) [$C_{(6)}n\cdots C_{(6)}n'$] ($\Delta R_{l\text{-}s}$) [Å] ($1 \le n \le 7$), measured for DFT optimized β-CD, HDM-β-CD, HMA-β-CD, and HDA-β-CD structures [B3LYP/6-31G(d); gas phase] using the Chimera version 1.16 program.

Parameter	β-CD	HDM-β-CD	HMA-β-CD	HDA-β-CD
$O_{(3)}nH\cdots O_{(2)}n'$ distance	1.879 ± 0.001			
$O_{(3)}n\text{-}H\cdots O_{(2)}n'$ angle	164.456 ± 0.041			
$O_{(6)}nH\cdots O_{(5)}n$ distance	2.324 ± 0.001	2.368 ± 0.055	2.389 ± 0.035	2.445 ± 0.117
$O_{(6)}n\text{-}H\cdots O_{(5)}n$ angle	106.736 ± 0.040	106.406 ± 1.019	104.879 ± 0.715	103.549 ± 1.948
$O_{(g)}n\cdots O_{(g)}n'$ $\Delta R_{l\text{-}s}$	0.006	1.948	1.181	1.839
$C_{(6)}n\cdots C_{(6)}n'$ $\Delta R_{l\text{-}s}$	0.013	8.125	5.135	4.462

Table 3. Isosurface area [Å^2], dipole moment [Debye], polarizability [au], zero-point vibrational energy (ZPVE) [kcal·mol^{-1}], standard deviation of quadrupole moment components (*Q* SD) [Debye-Å], dispersion energy contribution to the total electronic energy ($E_{disp.}$, *gd3bj* correction) [kcal·mol^{-1}], and solvation free energy ($\Delta G_{solvation}$) [kcal·mol^{-1}] calculated for the DFT optimized β-CD, HDM-β-CD, HMA-β-CD, and HDA-β-CD structures [B3LYP/6-31G(d); SMD, water].

Molecular properties	β-CD	HDM-β-CD	HMA-β-CD	HDA-β-CD
Isosurface Area	908.52	1133.18	1209.13	1351.80
Dipole moment	1.48	5.81	16.80	16.74
Polarizability	747.82	954.97	1069.99	1180.65
ZPVE	761.76	1010.74	1054.09	1096.18
Q SD (±)	2.30	11.41	34.00	74.29
E_{disp}	-205.39	-260.91	-300.01	-328.91
$\Delta G_{solvation}$	-84.80	-70.44	-97.01	-114.01

Table 4. DFT binding energies ($E_{binding}$), binding energy differences ($\Delta E_{binding}$), and EMO computed for the inclusion complexes of (*R*)- and (*S*)-tetramisole with β-CD, HDM-β-CD, HDA-β-CD, and HMA-β-CDs in the gas phase, with the SMD solvation, and with the *gd3* dispersion correction. The experimental EMO is reported for comparison.

		$E_{binding}$ (kcal·mol^{-1})	Tetramisole/CD			
CD	QM	(*R*)-complex	(*S*)-complex	$\Delta E_{binding}$ (kcal·mol^{-1})	$EMO_{calc.}$	$EMO_{exp.}$
β-CD	SMD	-6.69	-8.70	-2.01	(*R*)>(*S*)	(*R*)>(*S*)
HDM-β-CD	SMD	-15.57	-15.53	-0.04	(*S*)>(*R*)	ns[a]
HDA-β-CD	SMD/*gd3*	-40.88	-29.69	-11.19	(*S*)>(*R*)	(*S*)>(*R*)
HMA-β-CD	SMD/*gd3*	-36.77	-51.10	-14.33	(*R*)>(*S*)	(*R*)>(*S*)

[a]not separated

Table 5. Noncovalent interactions and related lengths (Å) observed in the inclusion complexes of (*R*)- and (*S*)-tetramisole with β-CD, HDM-β-CD, HDA-β-CD, and HMA-β-CDs computed at DFT level of theory.

		NCI[a]	Distance (Å)		
CD	QM	CD···enantiomer	(*R*)-complex	(*S*)-complex	EMO_{exp}
β-CD	SMD	**O(2)···H-N**	**1.861**		(*R*)>(*S*)
		O(3)···H-N		**1.754**	
		H(3)···H_{Ar}(*o*)	2.396	2.363	
		H(3)···H_{Ar}(*m*)		2.266, 2.300	
		H(5)···H_{Ar}(*m*)	2.704		
		H(5)···H_{Ar}(*m*)	2.594		
		H(5)···H_{Ar}(*p*)		2.912	
HDM-β-CD	SMD	OMe(3)···H-CHN	2.334	2.968	ns[b]
		OMe(2)···H-CHN		2.489	
		OMe(3)···H-N		2.394	
		H(3)-H···H-N	2.702		
		H(3)···H-CHN	2.560	2.457	
		H(3)···H-C*	2.781		
		H(3)···H_{Ar}(*o*)		2.366	
		H(5)···H_{Ar}(*m*)	2.338, 2.330	2.276, 2.415	
		H(5)···H_{Ar}(*o*)		2.674	
HDA-β-CD	SMD/*gd3*	**C=O(2)···H-N**	**1.854**	**2.011**	(*S*)>(*R*)
		OMe(2)···H-CHS	2.214		
		OMe(3)···H-CHN	2.193, 2.918		
		OMe(3)···H-C*	2.393		
		OMe(2)···H_{Ar}(*m*)		2.105	
		OMe(3)···H_{Ar}(*p*)		2.435	
		OMe(3)···H_{Ar}(*o*)	2.278	2.619	
		OMe(2)···H_{Ar}(*o*)	2.303		
		O(g)···H_{Ar}(*m*)	**2.353**		
		H(5)···H_{Ar}(*p*)	2.574		
		$HOCH_2$···H_{Ar}(*m*)	2.129		
HMA-β-CD	SMD/*gd3*	**O(g)···H-N**		**1.943**	(*R*)>(*S*)
		OMe(3)···H-CHS		2.676	
		OMe(3)···H-CHN	2.387, 2.535	2.233	
		OMe(2)···H-CHN		2.630	
		O(g)···H-CHN		**2.530**	
		OMe(3)···H-N	2.411		
		OMe(3)···H-C*	2.407		
		H(5)···H-C*		2.391	
		OMe(3)···H_{Ar}(*o*)	2.440	2.318	
		H(5)···H_{Ar}(*m*)		2.094	
		H(5)···H_{Ar}(*p*)	2.381	2.550	
		H(3)···H_{Ar}(*m*)	2.246		
		H(3)···H_{Ar}(*o*)	2.924		
		H(5)···H_{Ar}(*o*)		2.701	
		$HOCH_2$···H_{Ar}(*m*)	2.306		

[a]Noncovalent interactions, NCI
[b]not separated

Figure 1

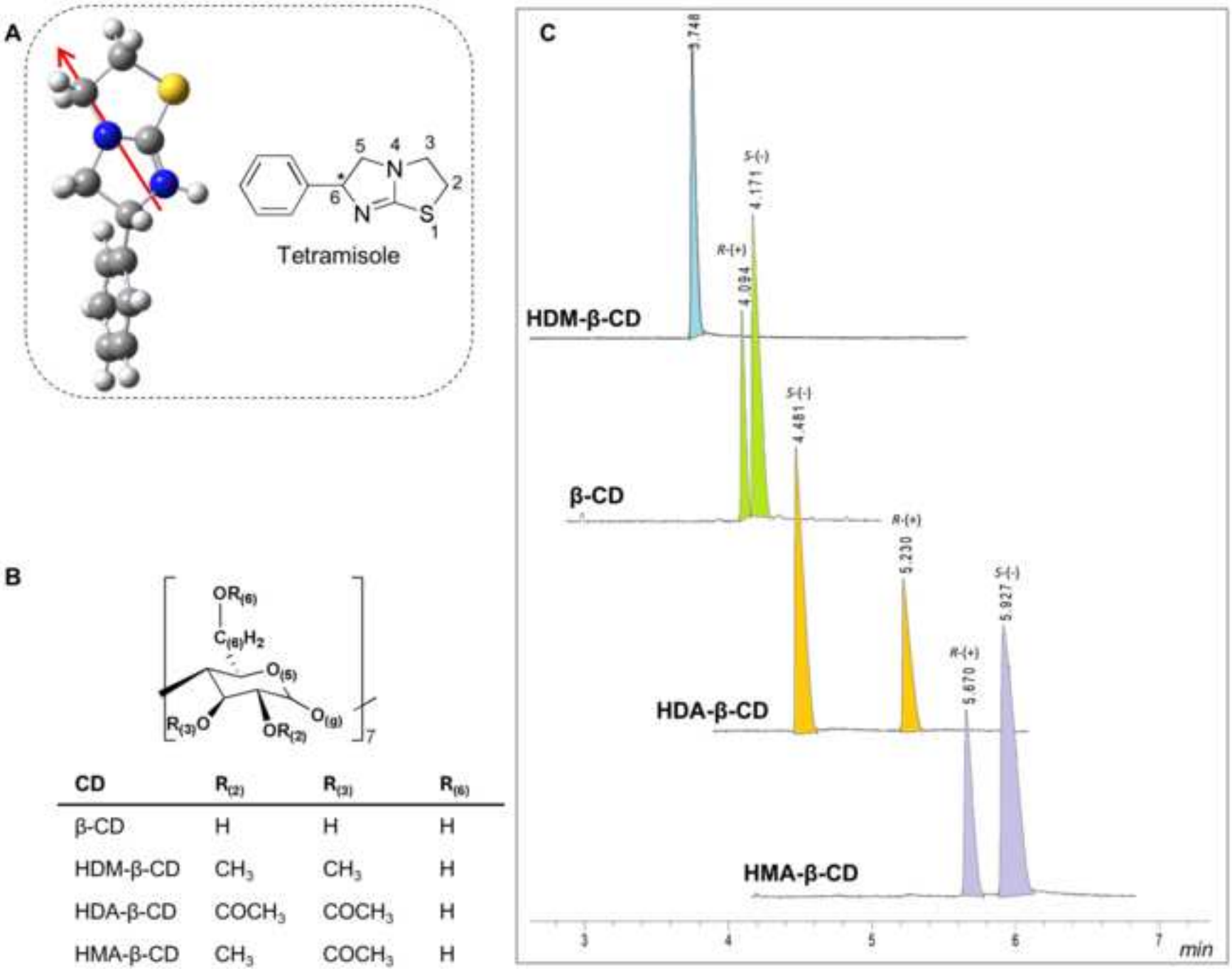

CD	$R_{(2)}$	$R_{(3)}$	$R_{(6)}$
β-CD	H	H	H
HDM-β-CD	CH_3	CH_3	H
HDA-β-CD	$COCH_3$	$COCH_3$	H
HMA-β-CD	CH_3	$COCH_3$	H

Figure 2

Click here to access/download;Figure(s);Figure 2.tif

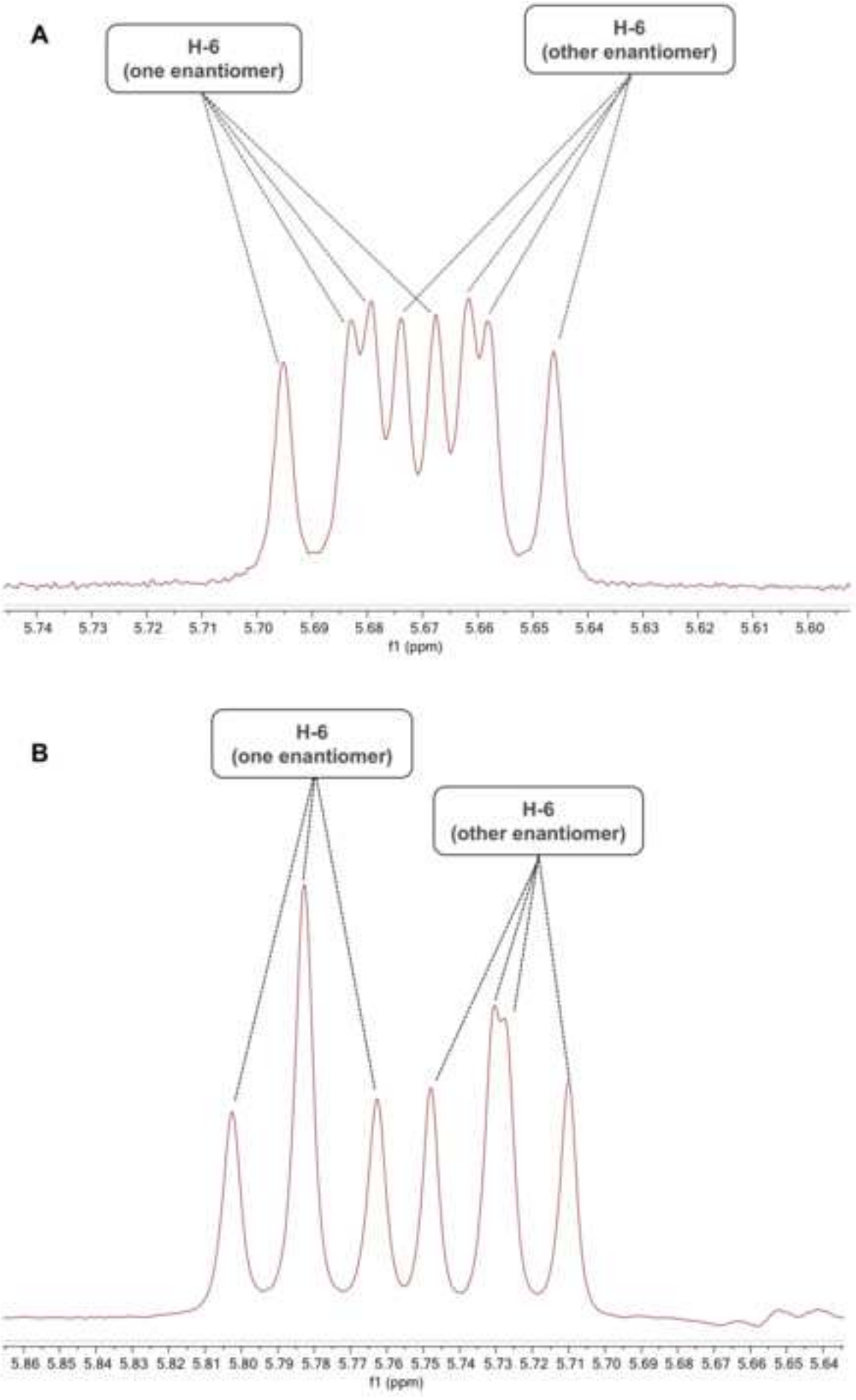

Figure 3

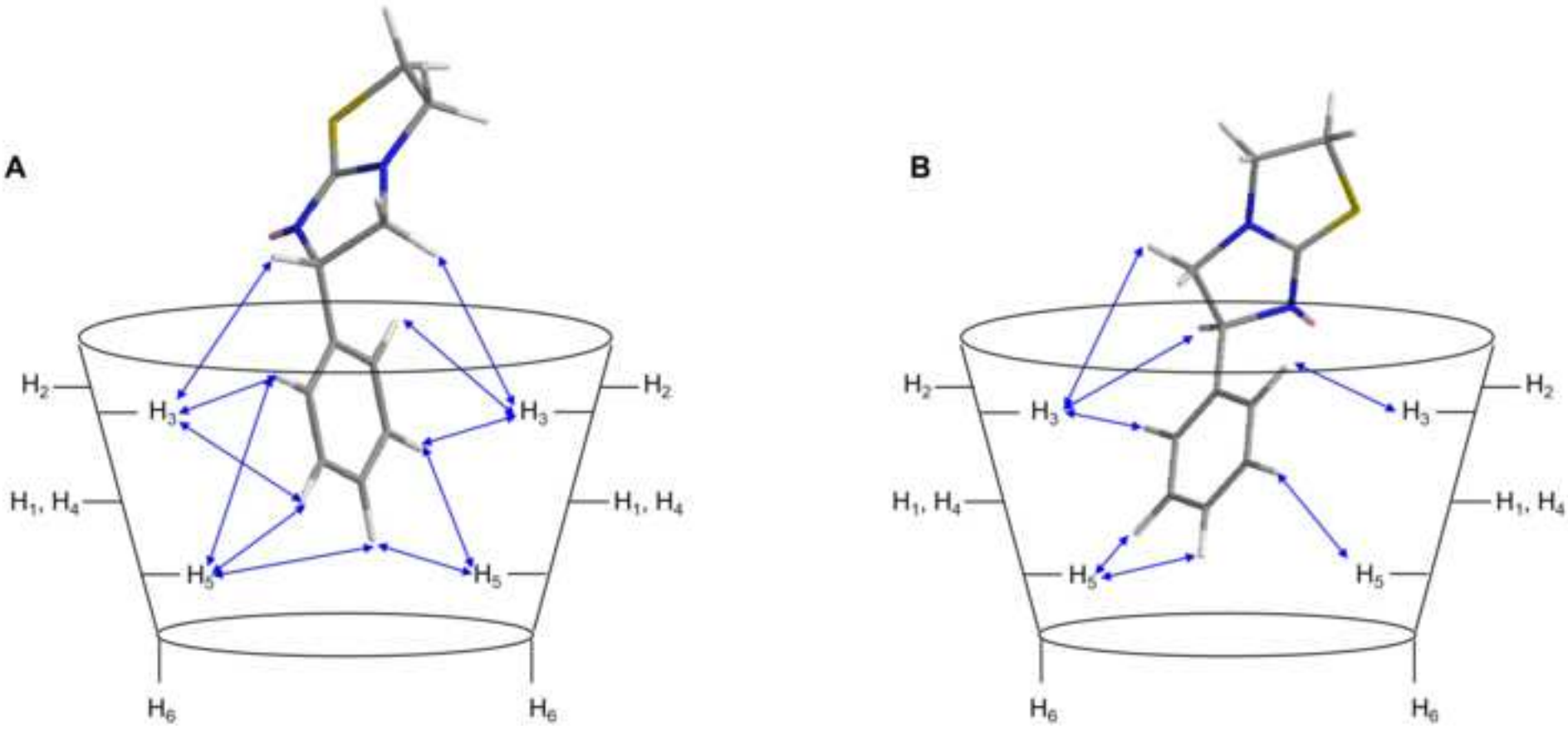

Figure 4

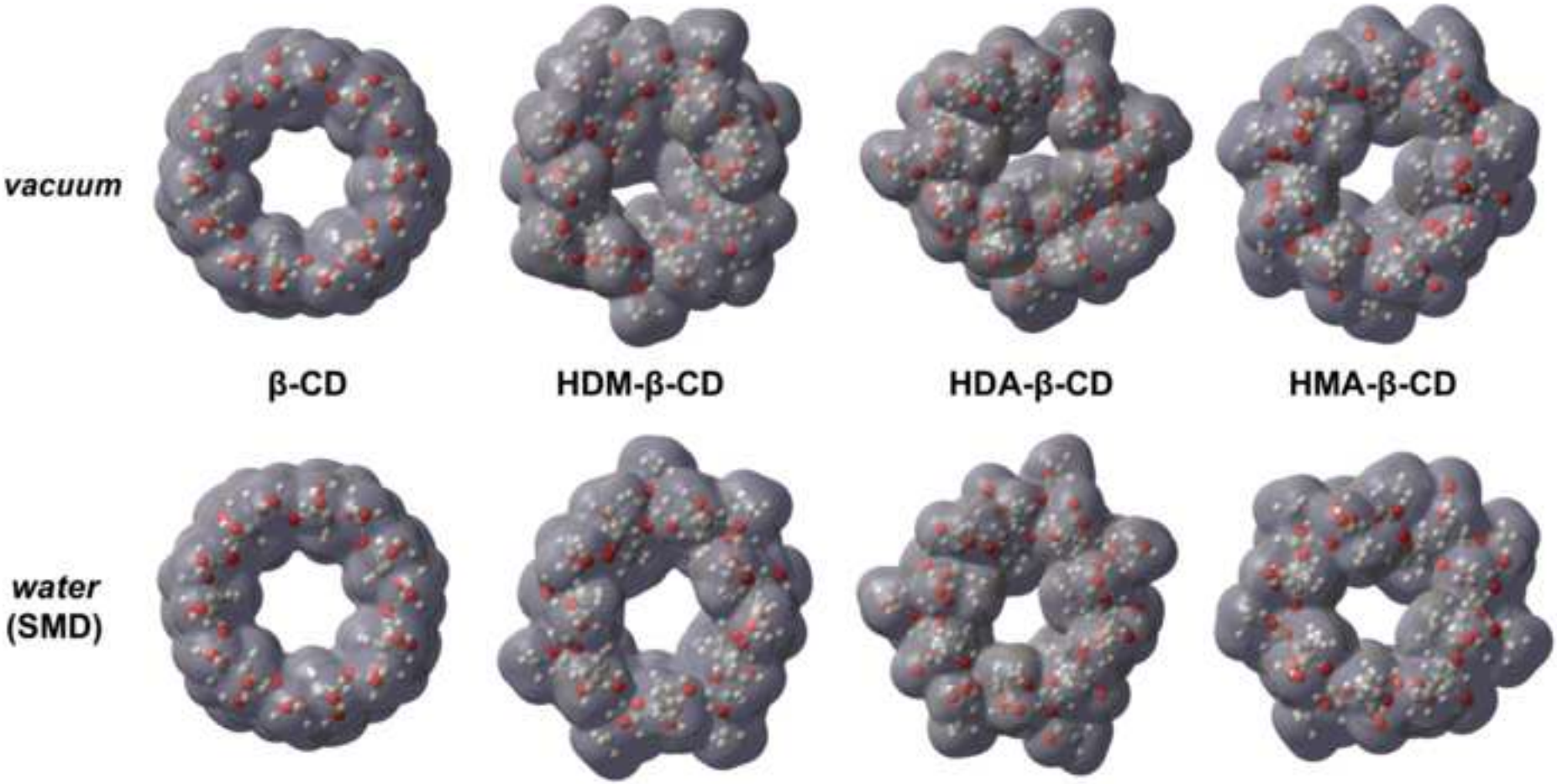

Figure 5

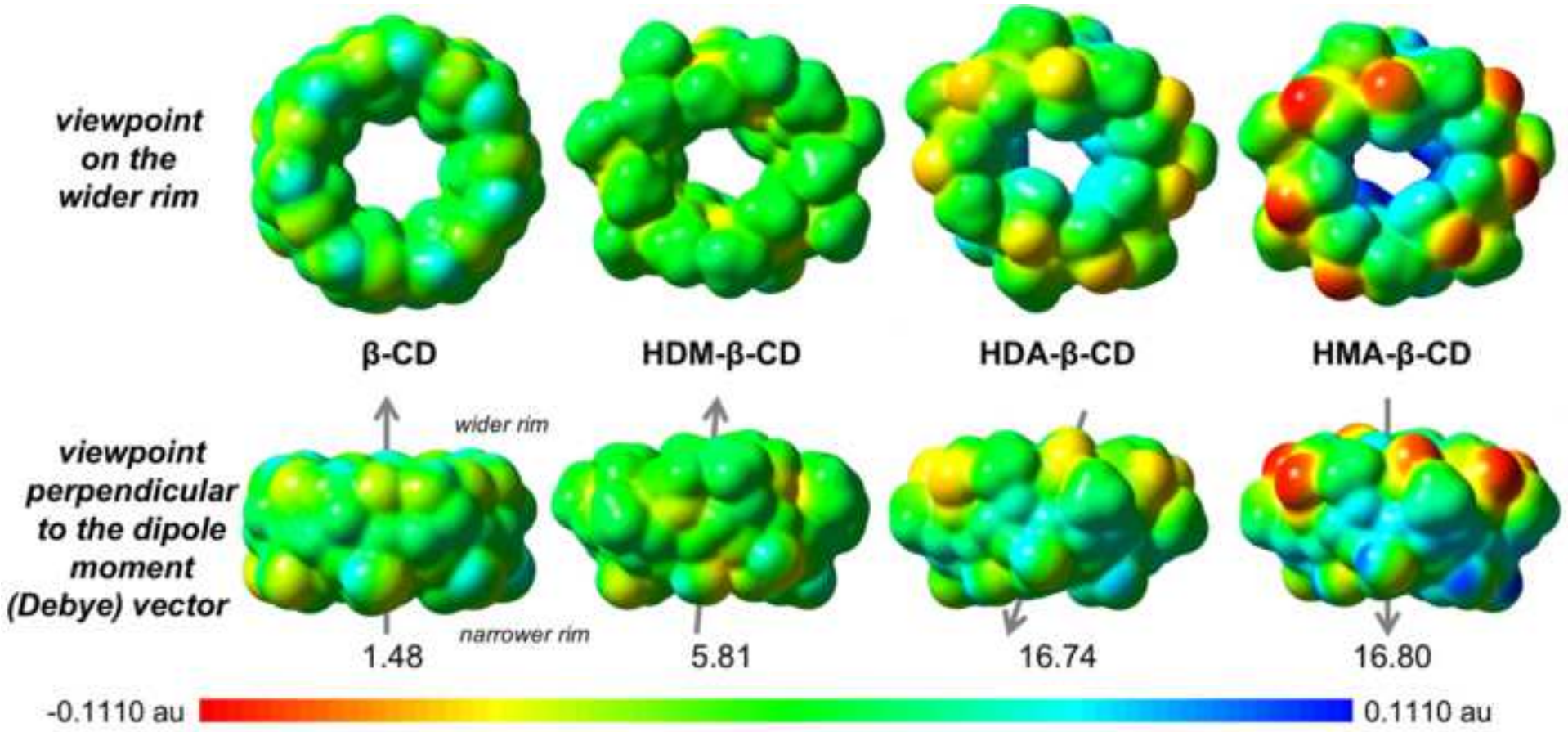

Figure 6

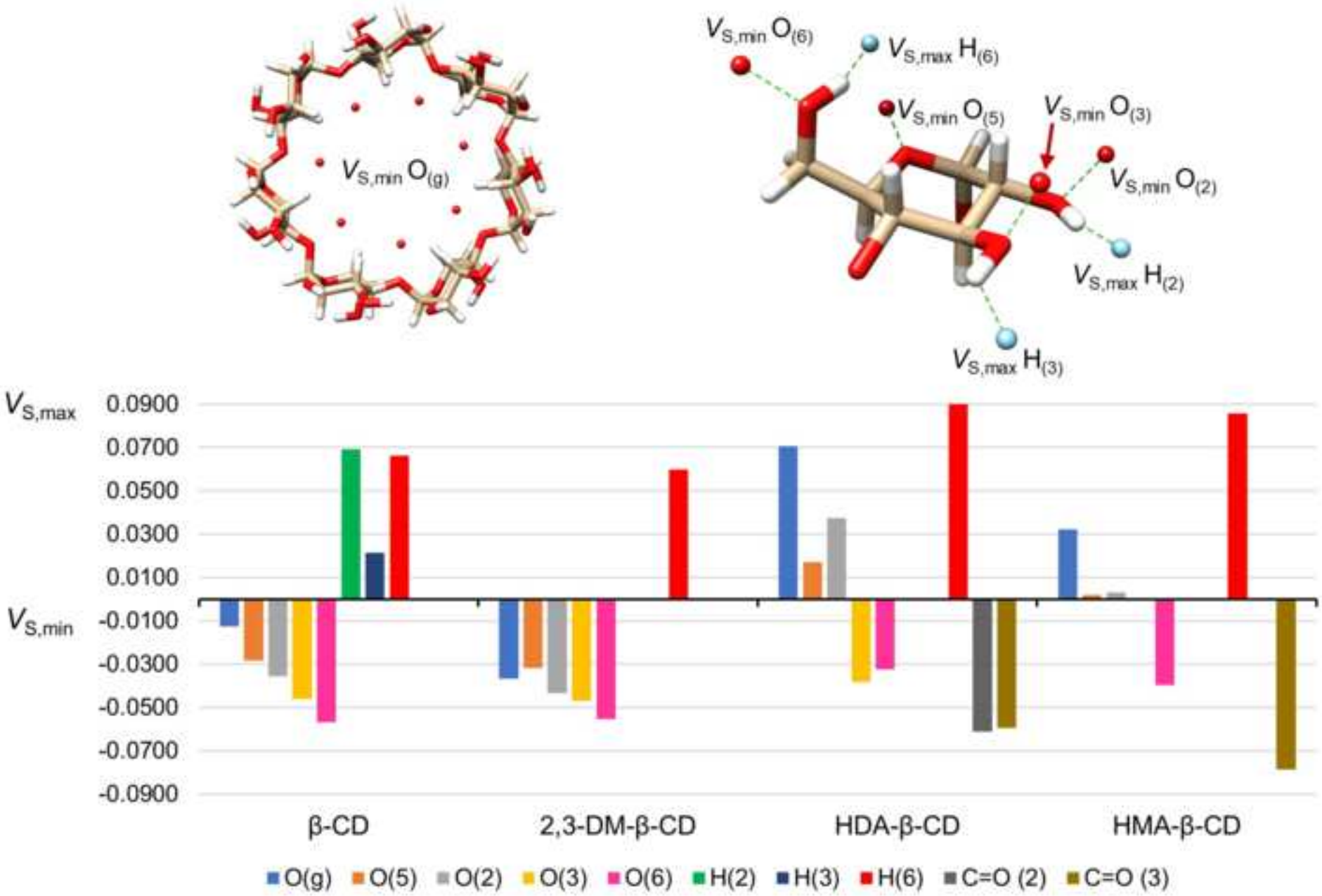

Figure 7

Click here to access/download;Figure(s);Figure 7.tif

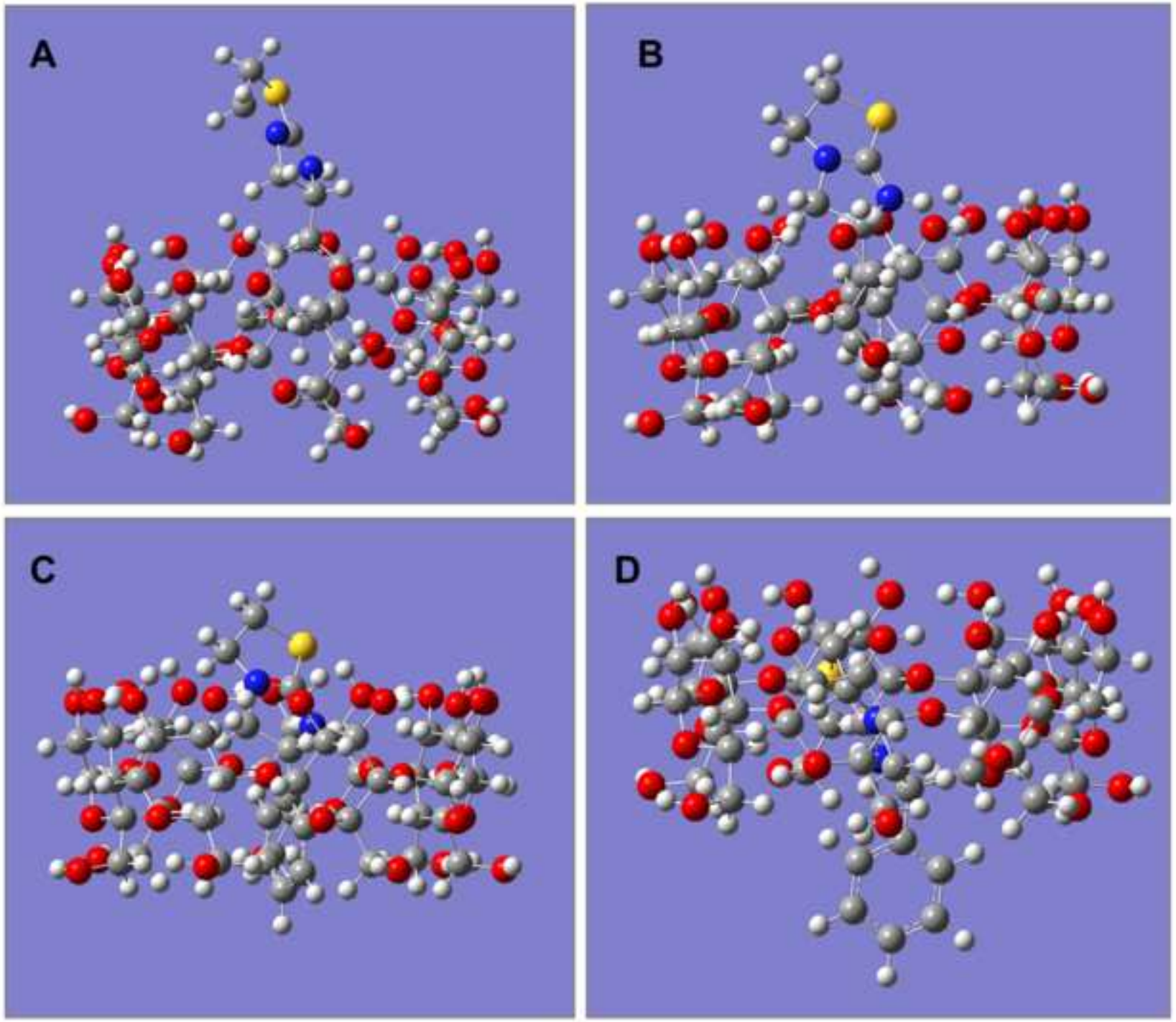

Figure 8

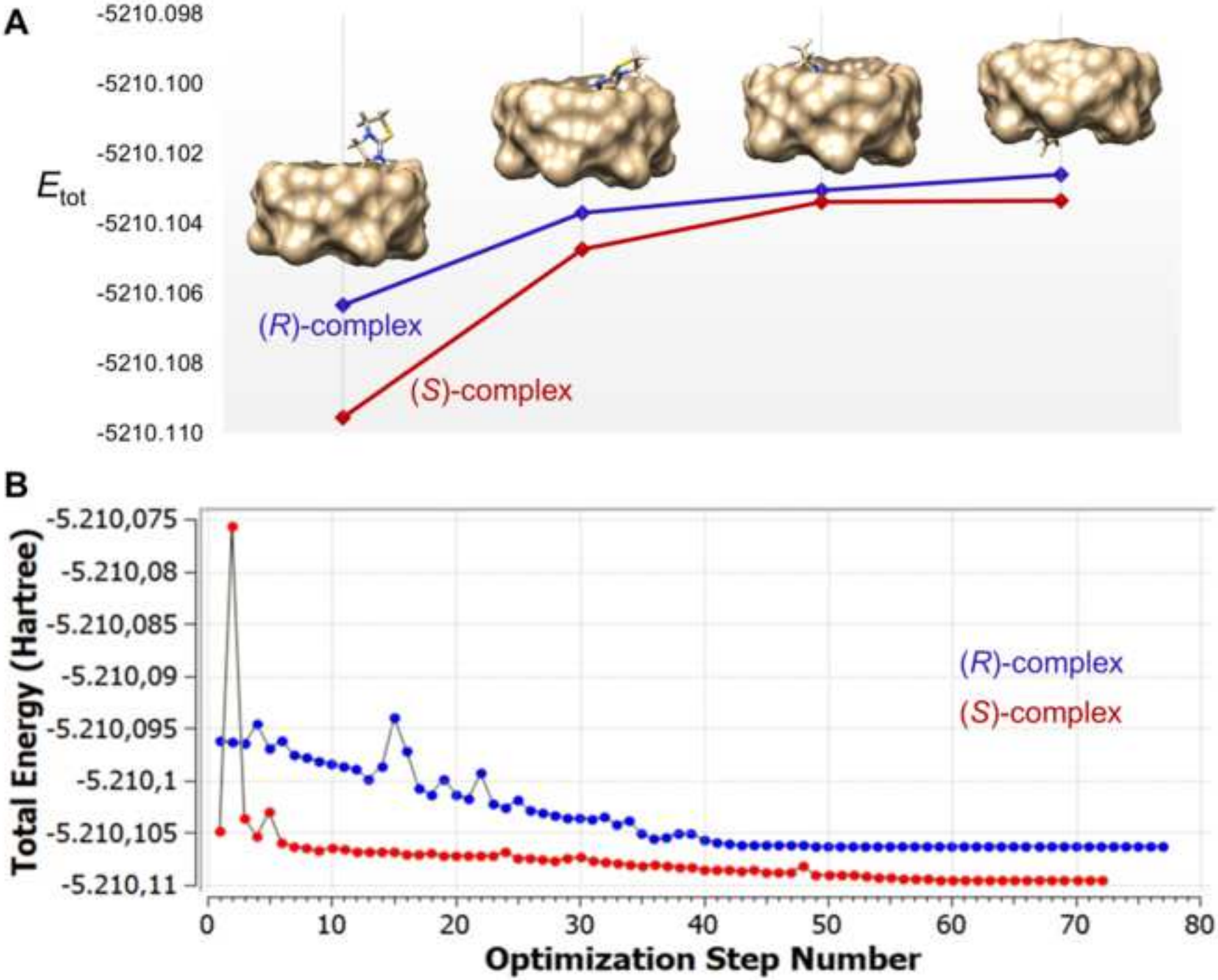

Figure 9

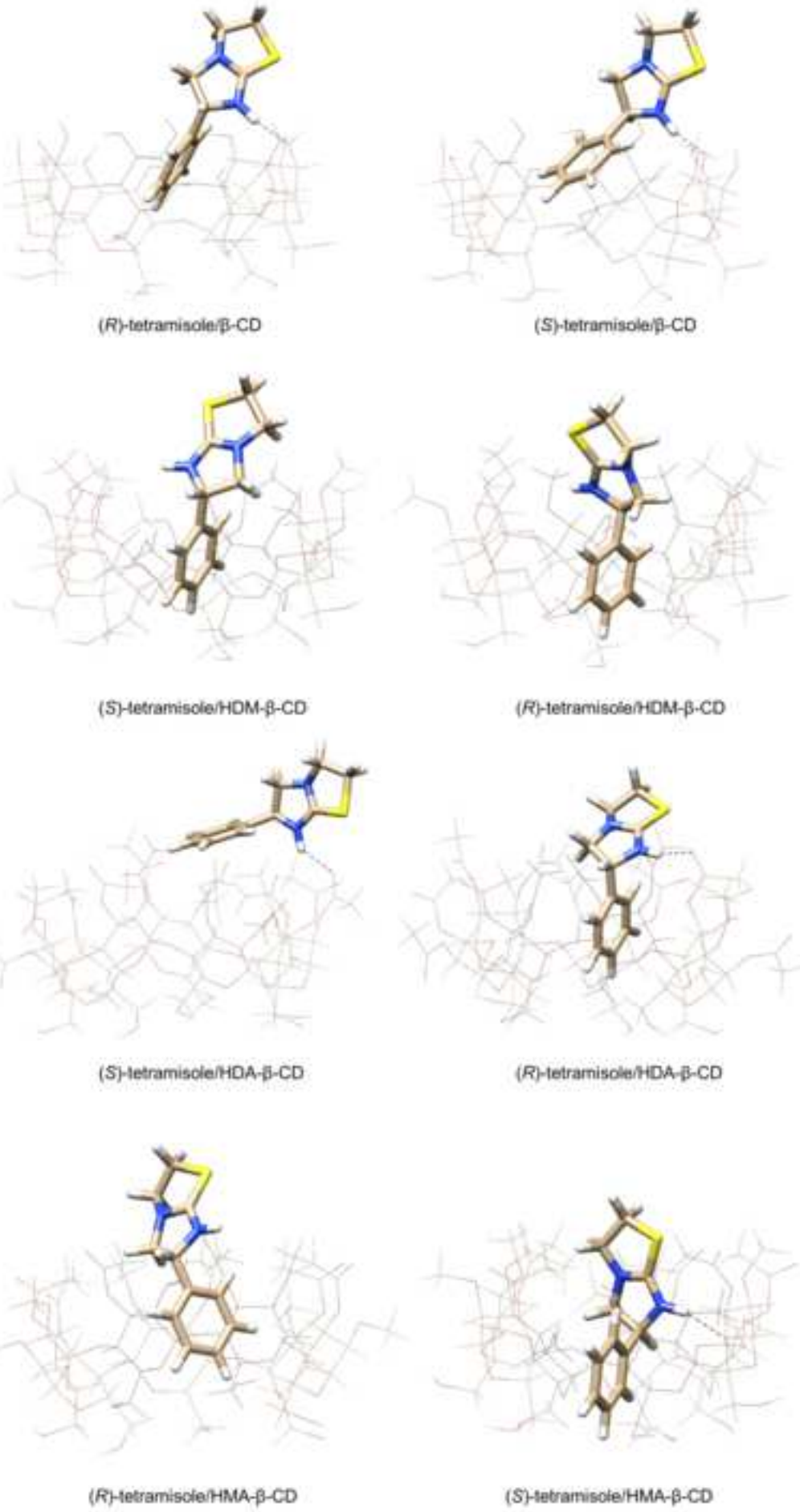

Figure 10

Click here to access/download;Figure(s);Figure 10.tif